Mechanically Tunable Lattice-Plasmon Resonances by Templated Self-Assembled Superlattices for Multi-Wavelength Surface-Enhanced Raman Spectroscopy

Mathias Charconnet, Christian Kuttner, Javier Plou, Juan Luis García-Pomar, Agustín Mihi, Luis M. Liz-Marzán,* and Andreas Seifert**

M. Charconnet, Prof. A. Seifert
CIC nanoGUNE BRTA, 20018 San Sebastián, Spain. E-mail: a.seifert@nanogune.eu

M. Charconnet, Dr. C. Kuttner, J. Plou, Prof. L. M. Liz-Marzán
CIC biomaGUNE, Basque Research and Technology Alliance (BRTA), 20014 Donostia-San Sebastián, Spain. E-mail: christian.kuttner@googlemail.com; llizmarzan@cicbiomagune.es

Dr. J. L. Garcia-Pomar
INL – International Iberian Nanotechnology Laboratory, 4715-330 Braga, Portugal

Dr. A. Mihi
Instituto de Ciencia de Materiales de Barcelona (ICMAB-CSIC), 08193 Bellaterra, Spain

Prof. L. M. Liz-Marzán, Prof. A. Seifert
IKERBASQUE - Basque Foundation for Science, Bilbao 48009, Spain

Prof. L. M. Liz-Marzán
Centro de Investigación en Red de Bioingeniería, Biomateriales y Nanomedicina (CIBER-BBN), 20014 Donostia-San Sebastián, Spain

Prof. L. M. Liz-Marzán
Department of Applied Chemistry, University of the Basque Country (EHU-UPV), 20018 San Sebastián, Spain

Keywords: plasmonics, template-assisted self-assembly, SERS, surface-enhanced Raman spectroscopy, lattice plasmons

Abstract (173 words): Lattice plasmons, *i.e.*, diffractively coupled localized surface plasmon resonances, occur in long-range ordered plasmonic nanostructures such as 1D and 2D periodic lattices. Such far-field coupled resonances can be employed for ultrasensitive surface-enhanced Raman spectroscopy (SERS), provided they are spectrally matched to the excitation wavelength. The spectral positions of lattice plasmon modes critically depend on the lattice period and uniformity, owing to their pronounced sensitivity to structural disorder. We report the fabrication of superlattices by templated self-assembly of gold nanoparticles on a flexible support, with tunable lattice-plasmon resonances by means of macroscopic strain. We

demonstrate that the highest SERS performance is achieved by matching the lattice plasmon mode to the excitation wavelength, by post-assembly fine-tuning of long-range structural parameters. Both asymmetric and symmetric lattice deformations can be used to adapt a single lattice structure to both red-shifted and blue-shifted excitation lines, as exemplified by lattice expansion and contraction, respectively. This proof-of-principle study represents a basis for alternative designs of adaptive functional nanostructures with mechanically tunable lattice resonances using strain as a macroscopic control parameter.

1. Introduction

Due to their remarkable ability to confine light to the nanoscale, plasmonic nanostructures are the preferred platform for ultrasensitive spectroscopy techniques, such as surface-enhanced Raman scattering (SERS) spectroscopy.[1,2] High and efficient signal enhancement typically demands a close match between the plasmon resonance wavelength and the excitation source.[3,4] Plasmon resonances can be engineered through nanostructure composition and morphology, as well as the refractive index of the environment.[5,6] In the case of superlattices, for example in the form of periodically arranged clusters of gold nanoparticles,[7] another control parameter comes into play, namely the lattice period. Lattice resonances result from diffractively coupled localized surface plasmons of a substructure within a periodic arrangement.[8] The periodicity, the center-to-center distance between adjacent plasmonic meta-atoms, is the key parameter for constructive (radiative) far-field coupling.

In the case of resonant excitation, lattice plasmons can generate intense electromagnetic fields,[9–11] as required for ultrasensitive SERS spectroscopy. We have recently shown that the resonance band of square-array 2D supercrystals, fabricated by template-assisted colloidal self-assembly of gold nanoparticles (NPs), can be tuned throughout the visible and near-infrared (NIR) range, as a function of the lattice parameter.[12] The highest SERS performance was achieved at best match with the laser excitation. Combining short- and long-range interactions

in such arrays can result in higher field enhancements. Tuning both the lattice period and the size of the substructures requires iterative remodeling of the template structure and its repeated fabrication by electron-beam lithography (EBL), which is time-consuming and costly. This issue makes mode matching a complex and tedious task that generally results in a trade-off between excitation efficiency and signal enhancement.

A key issue during fabrication is the rigid template that predetermines the plasmonic structure through the assembly procedure. We propose a more practical solution that allows for the subsequent modification of the lattice structure by physical or chemical external stimuli. Ideally, continuous and reversible tuning of the lattice periodicity would allow for a precise adjustment of the lattice resonance to the excitation wavelength of the laser, thus enabling a versatile screening of the most efficient SERS performance. Such a tunability could be achieved by changing the nanoscale spacing between gold nanoparticles within the substructures. In colloidal dispersions, dynamic tuning of plasmonic properties by distance control has already been demonstrated, for example through hydrophobic interactions,[13] pH, [14] or temperature variation.[15] In most cases, such control mechanisms cannot work on solid (rigid) substrates or under dry conditions. Alternatively, the substrate on which the nanostructure is supported would provide access to further tunability by using elastomeric materials[16] or through conformational changes of polymers under external stimuli.[17,18] Several studies have been reported on the manipulation of plasmonic modes in substrate-supported nanostructures by tuning near-field interactions between NPs.[19,20] For instance, Baumberg and coworkers used dark-field spectroscopy to demonstrate the controlled detuning of a single plasmonic dimer under mechanical strain.[21] Mechanical tuning of lattice plasmons has been applied to both all-dielectric[22] and plasmonic[23,24] lattice structures on stretchable supports. Expectations are high and numerous applications would benefit from the ability to implement active mechanical tuning, opening new avenues toward structural coloration with full-spectrum response,[25]

mechano-chromic materials,[26] nano-lasing,[23] programmable plasmon-mode engineering,[27]

and broadband metasurfaces[28] as multi-wavelength SERS substrates. Most of these approaches use top-down fabrication methods such as EBL, which offers excellent structural control on small areas. However, the current limits in scalability and resolution drive the search for bottom-up alternatives, such as nanostructuring by colloidal self-assembly.[29,30] Notwithstanding, nanostructures made of colloidal building blocks present additional challenges on flexible supports. In particular, the balance between adhesive and cohesive forces plays a major role during mechanical tuning of colloidal particle assemblies on elastomeric surfaces, as demonstrated by Steiner and coworkers.[31] Both detachment of the nanostructures from the support (adhesive failure) and structural fragmentation (cohesive failure) must be avoided by control of the interfacial chemistry.

Plasmonic nanostructures on elastomeric substrates show promising opportunities for next-generation sensing devices, realized by the combination of plasmonic tunability and mechanical flexibility.[32] This also holds true for bendable devices and sensing on non-planar material surfaces such as food,[33] plastics,[34] or textiles. However, purposefully oriented macroscopic mechanical strain as a fine-tuning tool for nanostructural parameters still poses a challenge for the precise control of plasmonic modes. We expect highest SERS performance under resonant excitation conditions, where the symmetry of the lattice deformation plays a critical role for constructive diffractive coupling. Thus, mode-matching by post-assembly adjustment of long-range structural parameters is expected to offer a relevant addition to near-field enhancements in plasmonic superlattices.

In particular, we present continuous and reversible tuning of lattice plasmon resonances by mechanical deformation of templated self-assembled gold NP superlattices on flexible substrates. As a proof of principle, we demonstrate the reversible mechanical tuning of a superlattice, made from a single template, for operation at two excitation wavelengths, using post-assembly lattice deformations. The effects of symmetric and asymmetric lattice deformations on the optical properties were studied under both unpolarized and linearly

polarized light. The SERS performance was confirmed to peak at resonant conditions, when the laser excitation coincides with the selected lattice modes. Mechanical strain thus serves as a macroscopic control parameter for the fine tuning of lattice resonances and their efficiency for multi-wavelength SERS.

2. Results and Discussion

2.1. Self-Assembly of Gold Nanoparticles into Superlattices

For the preparation of highly regular supercrystal arrays, we performed template-assisted colloidal self-assembly of spherical gold nanoparticles. This method has been previously reported for a variety of ordered structures, such as micron-sized square pyramids and hexagonally close-packed NP clusters.[10,11] Such superlattices have also been demonstrated to yield high SERS enhancement,[35] with applications, *e.g.*, for biosensing in complex media.[36] For the assembly, a drop of a colloidal dispersion of monodisperse gold nanospheres, stabilized with polyethylene glycol (PEG), is left to dry under confinement by a template mold made of polydimethylsiloxane (PDMS), as shown in **Figure 1**a. For experimental details, see Section S1 in the Supporting Information. Because in this study both the template and the target substrate were made of PDMS, it was necessary to apply a thin layer of polyethyleneimine (PEI) to promote particle transfer and adhesion onto the target substrate. By using PEI as adhesion promoter,[31] common problems regarding incomplete transfer could be efficiently avoided.

We worked with pre-patterned templates containing circular holes of 270 nm diameter and 115 nm depth, in a square grid with a period of 500 nm (Figure 1b). The resulting plasmonic superlattices consist of clusters, also called densely packed supercrystal substructures, within a regularly ordered arrangement that allows for intense far-field coupling.[8] The 500 nm periodicity was specifically chosen because it is an ideal structure for the proposed proof-of-concept in plasmonic tunability, where the corresponding lattice resonance is centered around

700 nm, hence between the two targeted excitation wavelengths of 633 and 785 nm, as shown in Figure 1c.

We prepared superlattices using gold nanospheres of different sizes, ranging from 30 to 105 nm in diameter; all of them assembled with the same lattice period of 500 nm (see Figure S1). Nanospheres of 40 nm diameter were found to yield the most suitable clusters, with high packing density and uniform cluster size. As an example, Figure 1d shows a photograph of a superlattice under white light illumination. At specific angles, an intense iridescent color can be observed due to light diffraction. Limited only by the size of the template, macroscale periodic arrangements of gold NPs were obtained over areas as large as one square centimeter. Due to the elastic nature of the PDMS substrate, it can be readily stretched or bent by mechanical deformation (see Figure 1e).

2.2. Superlattice Expansion and Compression

PDMS is a rubber-like elastic material with a Poisson's ratio near 0.5,[37] which is why it contracts in the directions transversal to the direction of strain. This feature can be used to expand and compress superlattices post-assembly. By stretching the PDMS-supported superlattice, a gradual color change can be observed by the naked eye (**Figure 2**a), which indicates a change of the period and thus of the diffracted wavelengths. Nonetheless, this visual indication gives no information about the state of the cluster substructures nor about the precise change of the lattice period. Indeed, different scenarios could take place under applied stress, such as detachment and slipping of the clusters on the substrate; changes in the interparticle gaps; or fragmentation[31] of the clusters into smaller units. Especially the latter two would induce dramatical changes in the resulting optical properties.[38] The balance between cohesive (particle-to-particle) and adhesive (particle-to-substrate) forces plays a critical role. If the cohesion between PEG-coated NPs is much larger than their adhesion to PEI-coated PDMS, the clusters can be expected to detach during stretching. In the reverse case, the applied stress

could break up the clusters, as was recently evidenced by mechanical simulations using the lattice spring model.[31] Both extreme cases must thus be avoided. Any structural changes to the cluster, including the number of NPs[39] and interparticle distances,[40] could have detrimental effects on lattice plasmons and SERS enhancement. Electromagnetic simulations confirm that even small changes in gap sizes within clusters would have a significant impact on the optical properties and near-field enhancement (Figure S8).

To study the structural changes of the superlattice upon mechanical deformation, environmental scanning electron microscopy (e-SEM) images were analyzed. Figure 2b and 2c compare the superlattice in the pristine/relaxed state and at 30% elongation. Please note, the observed dark vertical lines are artifacts due to charging during scanning (see also Figure S2). The lateral resolution of e-SEM imaging does not allow a direct quantification of interparticle distances within individual clusters (see Section S3). Nevertheless, statistical evaluation of the data obtained from image analysis yields reliable data for the relative change in interparticle distance when strain is applied. Figure S4d demonstrates that the interparticle gaps do not increase upon the mechanical deformation of the substrate. Neither fragmentation, break-up, nor any other significant conformational changes could be observed, even after repeated stretching cycles. Therefore, we conclude that the clusters are robust against the applied mechanical stress and that the balance between cohesion and adhesion is appropriate for tuning the lattice period. In addition, we determined the lattice periods of the superlattice from e-SEM images taken at different uniaxial elongations (Figure S3). At 30% elongation, the lattice periods in the horizontal and vertical directions changed from 500 nm to 645 nm and 440 nm, respectively. Figure 2d shows that the magnitude of the horizontal expansion is almost twice the vertical contraction, as expected for an incompressible rubber-like material with a Poisson's ratio near 0.5, such as PDMS.

2.3. Asymmetric Optical Tuning by Unidirectional Strain

Once we understood the conformational changes upon unidirectional strain, we focused our attention on the corresponding optical effects. Lattice plasmons rely on the constructive interference of scattered fields produced by the periodically arranged clusters.[8,41] The lattice plasmon wavelength of a square array can be estimated from the wavelength of in-plane diffracted orders λ_{diff}, also known as Rayleigh cutoff wavelengths, describing specific lattice effects, in analogy to so-called Wood's and Rayleigh's anomalies:[42,43]

$$\lambda_{diff}(m,p) = \frac{\sqrt{n_{sub}^2(m^2+p^2) - n_{top}^2 p^2 \sin^2(\theta)} \pm m\, n_{top} \sin(\theta)}{m^2+p^2} \cdot L \qquad (1)$$

The spectral position of this *lattice resonance effect* is determined by the period of the grating L, the refractive indices of interfacing media (substrate $n_{sub} \approx 1.40$-1.45 for PDMS[44] and superstrate $n_{top} = 1$ for air), and the angle of incidence θ.[45] The integers m and p correspond to the diffracted order. At normal incidence ($\theta = 0°$) the degenerated diffraction modes of first order (±1,0) and (0,±1) are given by:

$$\lambda_{diff}(\pm 1,0) = \lambda_{diff}(0, \pm 1) = n_{sub} \cdot L \qquad (2)$$

Thus, a square lattice with a period of 500 nm on a PDMS substrate corresponds to a diffraction mode[46] at 700 nm (asterisk in Figure 2e). To match the diffraction mode with the excitation lines at 633 and 785 nm, the grating period has to be reduced to ≈ 440 nm or extended to ≈ 550 nm, respectively. In fact, the diffraction mode could in principle be tuned even to an excitation line at 532 nm, corresponding to a lattice compression to ≈ 380 nm. However, for efficient transfer of energy from the incident light into the lattice plasmon, this anomaly must also energetically overlap with the plasmon resonance of the substructure,[8] *i.e.*, the self-assembled clusters.[47] Figure S5 shows the results of numerical calculations by the finite-difference time-domain (FDTD) method for the absorption cross section of an isolated cluster and the resulting broad resonance modes in the corresponding spectra (for details on modeling see Section S1). Only in the case of mutual resonance, there is an additional gain in the local

near-fields within the lattice,[9,12] as required for SERS (Figure S6). For that reason, the design of suitable lattice structures for efficient SERS excitation by mode matching is challenging, since several structural and optical parameters must be adjusted to each other at the same time. One can assume that asymmetric lattice deformations would result in optical anisotropy, with the coexistence of two separate grating anomalies in orthogonal directions. Each anomaly should be located at a distinct wavelength, either blue-shifted for lattice compression or red-shifted for lattice expansion (*cf.* Figure 2e). Control over the optical properties is important because they represent the basis for the excitation of electromagnetic hotspots and SERS in plasmonic nanostructures.[48,49] To better understand the influence of lattice variations on SERS measurements, first of all we need to correlate the optical properties with asymmetric deformations of the lattice. For this purpose, we performed UV/vis/NIR extinction spectroscopy in transmission geometry with a custom-made stretching device to study the changes in optical properties at a fixed sample position while applying unidirectional strain.

Figure 3 shows a UV/vis/NIR spectroscopic analysis under linearly polarized light, so that the influence on the optical spectra of both lattice modifications could be studied separately. The basic theory of plasmonic lattices states that for linearly polarized light and ideal orientation, the lattice plasmon excited along a principal direction should be plasmonically decoupled from the lattice plasmon in the perpendicular direction. However, depending on the structure of the subunits, near-field coupling effects can lead to transverse interactions. Polarization was adjusted along the direction of either expansion (Figure 3c,e) or compression (Figure 3d,f). For clarity, we used a simplified notation of *expansion mode* and *compression mode* below. The lattice plasmon of the superlattice in pristine/relaxed state builds on a grating anomaly (first-order diffractive mode), giving rise to a sharp extinction band around 710 nm, together with a shoulder at 530 nm. This peak is assigned mainly to a mixture of the plasmon mode for individual nanoparticles[50] and high-order longitudinal modes of the cluster, as shown in Figure S5.

Using light polarized along the axis of elongation, the lattice plasmon was found to redshift from 710 to 805 nm, for a lattice elongation of 35% (expansion mode, Figure 3c,e). If the incident light is polarized along the axis of compression, a lattice plasmon blueshift from 710 to 623 nm is observed instead (compression mode, Figure 3d,f). Hence, the polarization direction acts as a switch between both lattice plasmons. The evolution of the expansion and compression modes could also be reproduced by FDTD simulations, as shown in Figure 3e,f. Considering the multitude of parameters in this system (Section S1) and irregularities of the self-assembled clusters, the agreement between experimental and theoretical data is remarkable. Minor discrepancies can be attributed to the presence of more than a single cluster configuration in real samples, which is likely to influence the coupling efficiency to the lattice plasmon. In addition, for the sake of simplicity, the interparticle spacing in the simulations was fixed to 1 nm, set by a shell of refractive index of 1.46 to emulate PEG. Nevertheless, the evolution of the lattice modes upon lattice deformation is consistent with the experimental results. Figure 3g illustrates that the expansion mode is supported by the entire cluster, while the compression mode presents a mode profile that enhances mainly the field in the lateral part of the cluster (Figure 3h). The spectral position of the diffraction modes matches well with the position of the cluster modes in isolated state (Figure S5). The lattice mode thus hybridizes with the different cluster modes to form lattice plasmons depending on their spectral overlap.

Considering that both modes are close to the usual excitation lines of 633 and 785 nm, this model system renders our structures suitable for use under both SERS laser line excitations. It should be noted that, next to the expansion mode, a broad peak can be observed between 650 and 700 nm, likely due to plasmon modes for the cluster substructures, not coupling to the lattice. In other words, the progressive tuning of the grating anomaly (diffractive mode) toward the red leads to decoupling of the clusters from the lattice. This observation is supported by FDTD simulations, which predict a similar contribution for an isolated cluster of nanoparticles (Figure S5), with a broad band between 650 and 800 nm.

2.4. Symmetric Optical Tuning through Bidirectional Strain

We now have a clear understanding of the anisotropic optical response of asymmetrically deformed lattices. Since the plasmonic response strongly depends on the polarization state of the incoming light, the competition between transversal lattice plasmon modes may hinder the formation of efficient hotspots. Consequently, it would be advantageous to avoid symmetry breaking by applying a uniform strain in both directions. For this purpose, we used a custom-made two-dimensional stretching device. Here, the sample was clamped at all four sides, so that strain can be applied symmetrically. Because this device can only apply positive strain, the experiments were limited to (symmetric) optical tuning of the *expansion mode*.

Figure 4 compares the mode evolution for asymmetric (Figure 4a,c) and symmetric lattice deformations (Figure 4b,d). By performing optical measurements with unpolarized light, we observed that the asymmetric deformation mainly leads to a blueshift of the *compression mode* toward 633 nm. Though observable, the red-shifting *expansion mode* appears much weaker, which may be partly caused by the contribution of the cluster plasmon under non-resonant conditions to the lattice, as explained above. In addition, the imbalance between the number of compressed and extended cluster gaps within the measurement spot favors the *compression mode*. Because of the finite size of the illuminated area, lattice expansion is accompanied by a decrease in the number of sub-units with extended periods. On the contrary, lattice compression increases the number of sub-units with shorter periods within the probed area. To further support our understanding of the mode evolution, the same experiments were also carried out with a superlattice of 600 nm period (Figure S9 and S10). In this case, the pristine lattice plasmon was located at 840 nm, and the expansion mode shifted up to 930 nm at 30% elongation. The evolution of the modes observed during strain is fully consistent with our understanding, as detailed above.

Upon bidirectional symmetric stretching ($L_x = L_y$), a completely different optical behavior was observed. Figure 4d shows a pronounced *expansion mode* that progressively red-shifts (800 nm

at 20% elongation). A second spectral feature develops around 600 – 650 nm, which could be attributed to lattice plasmons formed by the (±1, ±1) diffractive mode (Figure 2e). The red-shift and the secondary feature are corroborated by FDTD simulations as shown in Figure S7. Upon bidirectional strain, the intensity of the *expansion mode* is much higher than that under unidirectional strain. This effect is in agreement with the understanding of the lattice plasmon, because coupling can take place more efficiently in a symmetric lattice, where both lattice parameters can diffract the excitation light efficiently.

We thus conclude that, bidirectional symmetric stretching is the method of choice to obtain an intense *expansion mode*, as exemplified here for square superlattices. We found that most of the experiments reported in the literature used unidirectional strain and thus considered asymmetric mechanical deformations.[24,27] Performing stretching experiments with bidirectional strain control allows us to avoid contraction of the sample and better controlled strain fields. Independent control over the periods in both axes allows for geometries that are not feasible with simple unidirectional stretching. To investigate the effect of symmetry on the optical properties of superlattices in more detail, we used a custom-made stretching device with separate control over both stretching axes. This allowed us to perform two-step stretching experiments: first, a square lattice was expanded into a rectangular lattice with a fixed vertical axis; the vertical axis was then gradually elongated to obtain a stretched square lattice. By stretching a square lattice into a rectangular one, we observed a redshift of the lattice plasmon, as expected. However, we also observed a significant broadening of the lattice mode (Figure S11). By stretching from a rectangular lattice into a stretched square lattice, an additional redshift of the *expansion mode* could be observed, but this time, the band became significantly sharper. A higher symmetry in superlattices leads to more intense and sharper lattice plasmon resonances, especially in the case of non-ideally aligned exciting fields or depolarized light, which is appealing for applications relying on high Q factors, such as nanolasing.[23] It is worth mentioning that a refractive-index matching layer[51,52] on top of the

plasmonic superlattices further decreases the spectral line width (Figure S12), which is however not an option regarding SERS applications.

On closer inspection, it is noticeable that the starting spectra (0%, black curves, Fig. 4e) for unidirectional and bidirectional stretching are not completely identical. The spectra differ by about 15 nm in their peak positions and the mode shapes are slightly different, which is due to the use of two different stretching devices. Whereas for unidirectional (asym.) stretching the sample was fixed on only two sides, for bidirectional (sym.) stretching all four sides had to be clamped to allow 2D deformations. Although all other measurement parameters were kept constant, owing to the two different clamping methods, slight differences in the 1D/2D pre-strain could not be entirely avoided. In combination with the high sensitivity of the optical properties to strain-induced deformations of the superstructure, minor variations in peak position and shape modulation of the lattice plasmon band are to be expected. Figure 4f compares the evolution of the lattice plasmons for asymmetric (blue squares) and symmetric deformations (red circles). For both methods of deformation, the *expansion modes* follow a linear trend for increasing elongation of the substrate. This behavior could be expected considering the linear relationship of the spectral position of the Rayleigh cutoff wavelength with the lattice period (*cf.* **Equation 2**, Figure 2e). The fact that both deformation methods yield almost identical plasmonic wavelengths, further supports the proposed concept of mechano-plasmonic tuning. This type of mode tuning is found to be fully reversible and could be validated by repeatedly switching between different elongation states with several stretching/release cycles (Figure S13).

2.5. SERS Performance of Strain-Deformed Superlattices

We finally investigated the impact of lattice tuning on SERS performance. Starting from the hypothesis that the best SERS performance relies on mode matching to the excitation laser,[12] resonance states can be expected for asymmetric elongation of 30 – 40% for 633 nm excitation,

and symmetric elongation of 10 – 20% for 785 nm excitation. To probe SERS enhancement, we used a low-molecular-weight model analyte, 4-nitrothiophenol (NTP), with a high affinity to adsorb onto gold and hydrophobic surfaces. Thus, the hydrophobicity of the PDMS support could be assumed to compete for the molecular adsorption of NTP. However, since the PDMS substrate was modified with PEI, its surface was rendered hydrophilic. For this reason, gold affinity should be the dominant factor here, driving the adsorption of the analyte into the hotspots between PEG-coated NPs. For more challenging analytes, *i.e.*, with lower adsorption affinity, the surface chemistry of the hotspots could be chemically adapted to the requirements of the analyte of interest. To avoid detrimental effects on the PDMS substrate, such as reduced elasticity, no additional cleaning steps were applied. It is well known that oxidized PDMS exhibits a brittle interface, which would undergo irreversible cracking when stretched. Labeling with NTP was carried out by drop-casting a freshly prepared 1 μM analyte solution, followed by washing with ethanol (Section S1). NTP is a widely used performance marker in SERS spectroscopy, due to its intense stretching vibration of the NO_2 group at 1330 cm^{-1}.

Figure 5 provides a summary of SERS experiments performed with both 633 and 785 nm excitation lasers, so as to investigate the effects of mode-matching by tuning the lattice parameters. The experiments were performed without an additional linear polarizer, so that it can be expected that the excitation light is partially depolarized by the Raman microscope optics. In principle, substrate stretching is accompanied by a decrease in the number of SERS emitters in the finite excitation volume (Figure S14) and thus a decrease in signal intensity could be expected. However, in the case of 633 nm excitation and unidirectional asymmetric stretching (Figure 5c), the Raman fingerprint remains almost constant up to an elongation of 30%. At 35%, when the lattice plasmon and the excitation laser are in resonance, the intensity increases significantly by 1.8 times by symmetric stretching and 3 times by asymmetric stretching (Figure 5e) – normalized to the intensity in unstretched state. Further stretching, however, causes a new loss of signal intensity, which confirms that SERS generated by the *compression*

mode is highly sensitive to changes in lattice period of ±25 nm (equivalent to ±5%). This is corroborated by numerical calculations of the dipole enhancement $|E|^2/|E_0|^2$ by the local electric field E_{loc} in the twofold amplification process, *i.e.*, the augmented excitation of a molecular dipole by an incident photon (λ_{exc}) and the stimulated emission of a scattered photon (λ_{sca}).[3,47]

$$EF = \frac{|E_{loc}(\lambda_{exc})|^2}{|E_0(\lambda_{exc})|^2} \times \frac{|E_{sca}(\lambda_{sca})|^2}{|E_0(\lambda_{sca})|^2} \quad (3)$$

This first-order approximation of the change in enhancement factors (EFs of $10^6 - 10^7$, Figure 5g, right axis) upon unidirectional strain is in excellent agreement with our experimental observations.

In the case of bidirectional symmetric stretching and 785 nm excitation (Figure 5d), a similar trend was also observed. After an initial damping up to 4% elongation, the signal intensity increased ca. 2-fold, with a maximum at 8-9% elongation, followed by a gradual decrease (Figure 5f). This behavior resembles the response curve of a resonance phenomenon, as one might expect for an excitation matching effect, also theoretically corroborated by FDTD simulations (Figure 5h). To test the repeatability of this effect, measurement cycles between different stretching states were performed (Figure S17). An excellent repeatability was found when switching between 0 and 8% elongation. Figure S18 compares the SERS performance at 785 nm of a superlattice, deformed by either asymmetric unidirectional strain or by symmetric bidirectional strain. Both types of stretching result in principle in the same expansion mode and in either case an additional gain in SERS performance can be observed upon resonant matching of the lattice plasmon with the excitation wavelength. However, the gain is more pronounced for symmetric deformations (Figure 5d), which further confirms our conclusion that the lattice plasmon generated via symmetric lattice tuning is more suitable for SERS applications due to its more uniform excitability.

To illustrate the importance of the lattice mode for increased SERS efficiency, a substrate without structural order was prepared for comparison. For this purpose, a drop of a colloidal

dispersion of Au nanospheres was drop-cast on PEI-coated PDMS without the spatial confinement of the nanostructured template. The resulting nanostructures consist of random domains (Figure S15), so that any influence from periodic order can be excluded. During stretching, the SERS signal was found to dramatically decrease using 785 nm excitation and stayed almost constant using 633 nm excitation (Figure S16). We attribute this behavior to a combination of the poorly excitable nanostructures as well as a decrease in the number of Raman marker molecules in the excitation volume upon stretching (Figure S14). For structured samples, the latter is compensated by the gain in enhancement upon excitation matching, which does not occur in the unorganized sample. Indeed, the optical properties of the unorganized sample (Figure S15) indicate a poorly defined plasmonic band, which did not show any significant changes upon stretching. We conclude that the hierarchical organization of the cluster into a periodic superstructure is the key to the observed SERS amplification. In both deformation scenarios, the highest gain in SERS performance was found by matching the lattice plasmon mode to the excitation wavelength, through fine-tuning of the lattice plasmon by post-assembly adjustment of long-range structural parameters.

Apart from the direct application of superlattices on flexible supports, the presented technology can be used for screening of structural parameters and identifying the most-suitable SERS conditions, *i.e.*, a contracted lattice of 450 nm for 633 nm excitation and an expanded lattice of 530 nm for 785 nm excitation. Unlike most SERS substrates that can only operate efficiently for a single excitation wavelength, mechanically tunable superlattices provide a broader useable excitation band. Within the spectral limits of the substructures' intrinsic plasmon bandwidth,[28] mechanical tuning grants access to multi-wavelength SERS substrates.

3. Conclusion

We demonstrated mechanical tuning of lattice plasmon resonances using a model system of self-assembled nanoparticle superlattices on a flexible substrate. This model system allows for a modulation of lattice periods using strain as a macroscopic control parameter. In this way, the structural parameters of the superstructures could be reversibly readjusted while keeping the plasmonic substructures intact. We assume that deformation of the lattice has a major effect on the inter-cluster distances as inferred from the optical spectra. Intra-cluster distances might be affected as well, but we propose, to a much lesser extent for the elongation rates considered. We support this hypothesis by the fact that elongated superlattices showed intense SERS signals emanating from the cluster substructures, indicating that such hotspots are still active upon deformation. We investigated the optical changes caused by expansion and contraction of the lattice, as a means for active mechanical tuning of plasmonic properties such as the control over the spectral position of the lattice plasmon. Here, we revealed the inherent differences between asymmetric and symmetric lattice deformations by a correlation of optical and structural parameters, which was faithfully reproduced by electromagnetic simulations. Rectangular lattice geometries were found to exhibit a competition between *compression* and *expansion modes*. As a proof of concept, we demonstrated that both lattice expansions and contractions can be used to adapt a single lattice structure to either red-shifted or blue-shifted excitation lines, respectively. An additional gain in SERS performance was observed when the lattice was tuned in resonance with the excitation, as initially hypothesized. Moreover, the gain in SERS performance relies on the resonant matching of the intrinsic plasmon band of the substructure (individual NP clusters) and the extrinsic diffraction mode of the superstructure (periodic arrangement), which constitutes the lattice plasmon. Consequently, the tuning range for efficient multi-wavelength SERS is predominantly limited by the spectral bandwidth of the substructure. The proposed technology serves for fast screening for most-suitable superlattice

designs and for guiding the development of other adaptive functional nanostructures with mechanically tunable optical properties.

Supporting Information

Supporting Information is available from the Wiley Online Library or from the author.

Acknowledgements

M.C. and C.K. contributed equally to this work. This work was supported by the Spanish Ministry of Economy, Industry, and Competitiveness under the Maria de Maeztu and Severo Ochoa Units of Excellence Programme – MDM-2016-0618 , MDM-2017-0720, and FUNFUTURE (CEX2019-000917-S); by the Basque Government in the Elkartek Program 2020/21; by the Spanish Ministerio de Ciencia e Innovación (PID2019-106860GB-I00); by the European Union's Horizon 2020 research and innovation program under the Marie Skłodowska-Curie grant agreement no. 799393 (NANOBIOME); Marie Skłodowska-Curie grant agreement no. 840064 (2D_PHOT); and by the European Research Council (ERC-AdG-2017 no. 787510, 4DbioSERS). The authors thank Dr. Judith Langer for scientific discussions and Eneko Lopez for the design and additive manufacturing of the 2D stretching device.

Conflict of Interest

There are no financial/commercial Conflicts of Interest to declare. The manuscript was written through contributions of all authors. All authors have given approval to the final version of the manuscript.

Received: ((will be filled in by the editorial staff))
Revised: ((will be filled in by the editorial staff))
Published online: ((will be filled in by the editorial staff))

References

[1] J. Langer, D. Jimenez de Aberasturi, J. Aizpurua, R. A. Alvarez-Puebla, B. Auguié, J. J. Baumberg, G. C. Bazan, S. E. J. Bell, A. Boisen, A. G. Brolo, J. Choo, D. Cialla-May, V. Deckert, L. Fabris, K. Faulds, F. J. García de Abajo, R. Goodacre, D. Graham, A. J. Haes, C. L. Haynes, C. Huck, T. Itoh, M. Käll, J. Kneipp, N. A. Kotov, H. Kuang, E. C. Le Ru, H. K. Lee, J.-F. Li, X. Y. Ling, S. A. Maier, T. Mayerhöfer, M. Moskovits, K. Murakoshi, J.-M. Nam, S. Nie, Y. Ozaki, I. Pastoriza-Santos, J. Perez-Juste, J. Popp, A. Pucci, S. Reich, B. Ren, G. C. Schatz, T. Shegai, S. Schlücker, L.-L. Tay, K. G. Thomas, Z.-Q. Tian, R. P. Van Duyne, T. Vo-Dinh, Y. Wang, K. A. Willets, C. Xu, H. Xu, Y. Xu, Y. S. Yamamoto, B. Zhao, L. M. Liz-Marzán, *ACS Nano* **2020**, *14*, 28.

[2] C. Hamon, M. N. Sanz-Ortiz, E. Modin, E. H. Hill, L. Scarabelli, A. Chuvilin, L. M. Liz-Marzán, *Nanoscale* **2016**, *8*, 7914.

[3] C. Kuttner, In *Plasmonics* (Ed.: Gric, T.), IntechOpen, **2018**, pp. 151–180.

[4] D. Graham, R. Goodacre, H. Arnolds, J. F. Masson, G. Schatz, J. Baumberg, D. H. Kim, J. Aizpurua, W. Lum, A. Silvestri, B. De Nijs, Y. Xu, G. Di Martino, M. Natan, S. Schlücker, P. Wuytens, I. Bruzas, C. Kuttner, M. Hardy, R. Chikkaraddy, N. Martín Sabanés, I. Delfino, P. Dawson, S. Gawinkowski, N. Bontempi, S. Mahajan, S. Reich, B. Hourahine, S. Bell, A. Królikowska, M. Porter, A. Keeler, M. Kamp, A. Fountain, C. Fasolato, F. Giorgis, J. C. Otero, C. Matricardi, R. Van Duyne, J. Lombardi, V. Deckert, L. Velleman, *Faraday Discuss.* **2017**, *205*, 173.

[5] M. B. Müller, C. Kuttner, T. A. F. König, V. V. Tsukruk, S. Förster, M. Karg, A. Fery, *ACS Nano* **2014**, *8*, 9410.

[6] K. Volk, J. P. S. Fitzgerald, P. Ruckdeschel, M. Retsch, T. A. F. König, M. Karg, *Adv. Opt. Mater.* **2017**, *5*, 1600971.

[7] M. Karg, T. Hellweg, P. Mulvaney, *Adv. Funct. Mater.* **2011**, *21*, 4668.

[8] V. G. Kravets, A. V. Kabashin, W. L. Barnes, A. N. Grigorenko, *Chem. Rev.* **2018**, *118*, 5912.

[9] J. Černigoj, F. Silvestri, L. P. Stoevelaar, J. Berzinš, G. Gerini, *Sci. Rep.* **2018**, *8*, 15706.

[10] C. Hanske, G. González-Rubio, C. Hamon, P. Formentín, E. Modin, A. Chuvilin, A. Guerrero-Martínez, L. F. Marsal, L. M. Liz-Marzán, *J. Phys. Chem. C* **2017**, *121*, 10899.

[11] C. Hanske, E. H. Hill, D. Vila-Liarte, G. González-Rubio, C. Matricardi, A. Mihi, L. M. Liz-Marzán, *ACS Appl. Mater. Interfaces* **2019**, *11*, 11763.

[12] C. Matricardi, C. Hanske, J. L. Garcia-Pomar, J. Langer, A. Mihi, L. M. Liz-Marzán, *ACS Nano* **2018**, *12*, 8531.

[13] A. Sánchez-Iglesias, M. Grzelczak, T. Altantzis, B. Goris, J. Pérez-Juste, S. Bals, G. Van Tendeloo, S. H. Donaldson, B. F. Chmelka, J. N. Israelachvili, L. M. Liz-Marzán, *ACS Nano* **2012**, *6*, 11059.

[14] P. Taladriz-Blanco, N. J. Buurma, L. Rodríguez-Lorenzo, J. Pérez-Juste, L. M. Liz-Marzán, P. Hervés, *J. Mater. Chem.* **2011**, *21*, 16880.

[15] J. Kruse, S. Merkens, A. Chuvilin, M. Grzelczak, *ACS Appl. Nano Mater.* **2020**, *3*, 9520.

[16] R. M. Cole, S. Mahajan, J. J. Baumberg, *Appl. Phys. Lett.* **2009**, *95*, 154103.

[17] J. Peng, H.-H. Jeong, Q. Lin, S. Cormier, H.-L. Liang, M. F. L. De Volder, S. Vignolini, J. J. Baumberg, *Sci. Adv.* **2019**, *5*, eaaw2205.

[18] I. Tokareva, S. Minko, J. H. Fendler, E. Hutter, *J. Am. Chem. Soc.* **2004**, *126*, 15950.

[19] H. Kang, C. J. Heo, H. C. Jeon, S. Y. Lee, S. M. Yang, *ACS Appl. Mater. Interfaces* **2013**, *5*, 4569.

[20] S. Aksu, M. Huang, A. Artar, A. A. Yanik, S. Selvarasah, M. R. Dokmeci, H. Altug, *Adv. Mater.* **2011**, *23*, 4422.

[21] F. Huang, J. J. Baumberg, *Nano Lett.* **2010**, *10*, 1787.

[22] C. Zhang, J. Jing, Y. Wu, Y. Fan, W. Yang, S. Wang, Q. Song, S. Xiao, *ACS Nano* **2020**, *14*, 1418.

[23] D. Wang, M. R. Bourgeois, W. K. Lee, R. Li, D. Trivedi, M. P. Knudson, W. Wang, G. C. Schatz, T. W. Odom, *Nano Lett.* **2018**, *18*, 4549.

[24] Y. Brasse, V. Gupta, H. C. T. Schollbach, M. Karg, T. A. F. König, A. Fery, *Adv. Mater. Interfaces* **2020**, *7*, 1901678.

[25] M. L. Tseng, J. Yang, M. Semmlinger, C. Zhang, P. Nordlander, N. J. Halas, *Nano Lett.* **2017**, *17*, 6034.

[26] L. Minati, A. Chiappini, C. Armellini, A. Carpentiero, D. Maniglio, A. Vaccari, L. Zur, A. Lukowiak, M. Ferrari, G. Speranza, *Mater. Chem. Phys.* **2017**, *192*, 94.

[27] A. Yang, A. J. Hryn, M. R. Bourgeois, W. K. Lee, J. Hu, G. C. Schatz, T. W. Odom, *Proc. Natl. Acad. Sci. U. S. A.* **2016**, *113*, 14201.

[28] N. Zhang, K. Liu, Z. Liu, H. Song, X. Zeng, D. Ji, A. Cheney, S. Jiang, Q. Gan, *Adv. Mater. Interfaces* **2015**, *2*, 1500142.

[29] C. Kuttner, M. Chanana, M. Karg, A. Fery, In *Macromolecular Self-assembly* (Eds.: Billon, L.; Borisov, O.), **2016**, pp. 159–192.

[30] C. Hanske, M. Tebbe, C. Kuttner, V. Bieber, V. V. Tsukruk, M. Chanana, T. A. F. König, A. Fery, *Nano Lett.* **2014**, *14*, 6863.

[31] A. M. Steiner, M. Mayer, M. Seuss, S. Nikolov, K. D. Harris, A. Alexeev, C. Kuttner, T. A. F. König, A. Fery, *ACS Nano* **2017**, *11*, 8871.

[32] K. Xu, R. Zhou, K. Takei, M. Hong, *Adv. Sci.* **2019**, *6*.

[33] A. Shiohara, J. Langer, L. Polavarapu, L. M. Liz-Marzán, *Nanoscale* **2014**, *6*, 9817.

[34] P.-Y. Lin, C.-W. Hsieh, S. Hsieh, *Sci. Rep.* **2017**, *7*, 16698.

[35] G. Bodelón, V. Montes-García, C. Costas, I. Pérez-Juste, J. Pérez-Juste, I. Pastoriza-Santos, L. M. Liz-Marzán, *ACS Nano* **2017**, *11*, 4631.

[36] J. Plou, I. García, M. Charconnet, I. Astobiza, C. García-Astrain, C. Matricardi, A. Mihi, A. Carracedo, L. M. Liz-Marzán, *Adv. Funct. Mater.* **2020**, *30*, 1910335.

[37] S. Dogru, B. Aksoy, H. Bayraktar, B. E. Alaca, *Polym. Test.* **2018**, *69*, 375.

[38] H. Mitomo, K. Horie, Y. Matsuo, K. Niikura, T. Tani, M. Naya, K. Ijiro, *Adv. Opt. Mater.* **2016**, *4*, 259.

[39] J. A. Fan, K. Bao, L. Sun, J. Bao, V. N. Manoharan, P. Nordlander, F. Capasso, *Nano Lett.* **2012**, *12*, 5318.

[40] P. K. Jain, W. Huang, M. A. El-Sayed, *Nano Lett.* **2007**, *7*, 2080.

[41] M. B. Ross, C. A. Mirkin, G. C. Schatz, *J. Phys. Chem. C* **2016**, *120*, 816.

[42] A. Hessel, A. A. Oliner, *Appl. Opt.* **1965**, *4*, 1275.

[43] A. D. Humphrey, W. L. Barnes, *J. Opt.* **2016**, *18*, 035005.

[44] V. Gupta, P. T. Probst, F. R. Goßler, A. M. Steiner, J. Schubert, Y. Brasse, T. A. F. König, A. Fery, *ACS Appl. Mater. Interfaces* **2019**, *11*, 28189.

[45] D. Khlopin, F. Laux, W. P. Wardley, J. Martin, G. A. Wurtz, J. Plain, N. Bonod, A. V. Zayats, W. Dickson, D. Gérard, *J. Opt. Soc. Am. B* **2017**, *34*, 691.

[46] V. G. Kravets, F. Schedin, A. N. Grigorenko, *Phys. Rev. Lett.* **2008**, *101*, 087403.

[47] J. C. Fraire, L. A. Pérez, E. A. Coronado, *J. Phys. Chem. C* **2013**, *117*, 23090.

[48] R. P. M. M. Höller, C. Kuttner, M. Mayer, R. Wang, M. Dulle, R. Contreras-Cáceres, A. Fery, L. M. Liz-Marzán, *ACS Photonics* **2020**, *7*, 1839.

[49] V. Tran, C. Thiel, J. T. Svejda, M. Jalali, B. Walkenfort, D. Erni, S. Schlücker, *Nanoscale* **2018**, *10*, 21721.

[50] D. Dregely, M. Hentschel, H. Giessen, *ACS Nano* **2011**, *5*, 8202.

[51] B. D. Thackray, V. G. Kravets, F. Schedin, G. Auton, P. A. Thomas, A. N. Grigorenko, *ACS Photonics* **2014**, *1*, 1116.

[52] E. Ponomareva, K. Volk, P. Mulvaney, M. Karg, *Langmuir* **2020**, *36*, 13601.

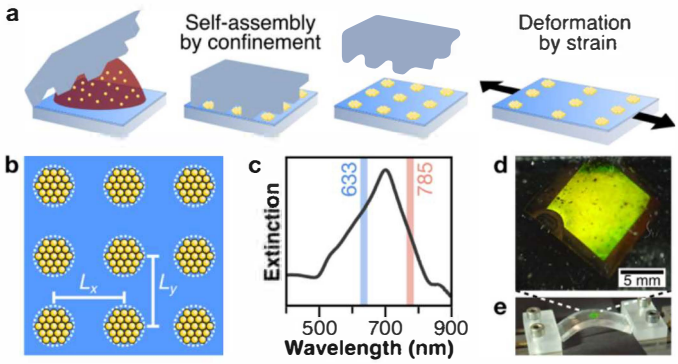

(89 × 47 mm^2, 300 dpi)

Figure 1. Colloidal fabrication of superlattices on flexible supports: (a) Templated self-assembly of plasmonic superlattices onto a PEI-coated PDMS substrate, which can be stretched by application of macroscopic strain. (b) Schematic representation of the superlattice design with indicated lattice periods in horizontal L_x and vertical direction L_y, as indicated. (c) Experimental extinction spectra of transmitted light in the relaxed state. Photographs of the superlattice under white-light illumination in the relaxed (d) and bent (e) states. The green iridescent color results from light diffraction.

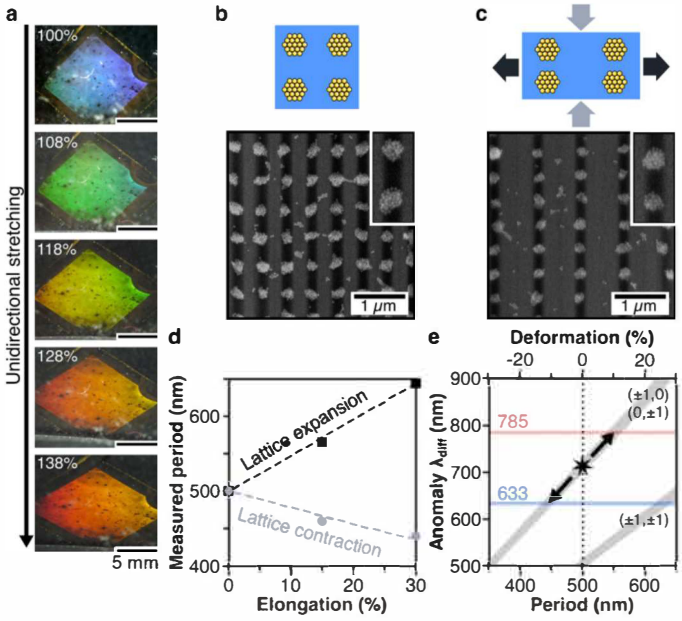

(89 × 81 mm^2, 300 dpi)

Figure 2. Tuning of lattice period: (a) Digital photographs of a superlattice on PDMS under unidirectional stretching and white-light illumination, showing light diffraction by the grating structure. A gradual color change is observed upon stretching. (b,c) Schematic drawings and environmental e-SEM images of a 500 nm superlattice in the pristine state (b) and elongated by 30% (c). (d) Changes in the horizontal (black squares) and vertical periods (gray circles) under unidirectional strain, evaluated from e-SEM images. Dashed lines are guides to the eye. (e) Calculated spectral position of diffraction anomalies (gray) at normal incidence, as a function of lattice period, predicted by lattice theory (**Equation 1**).

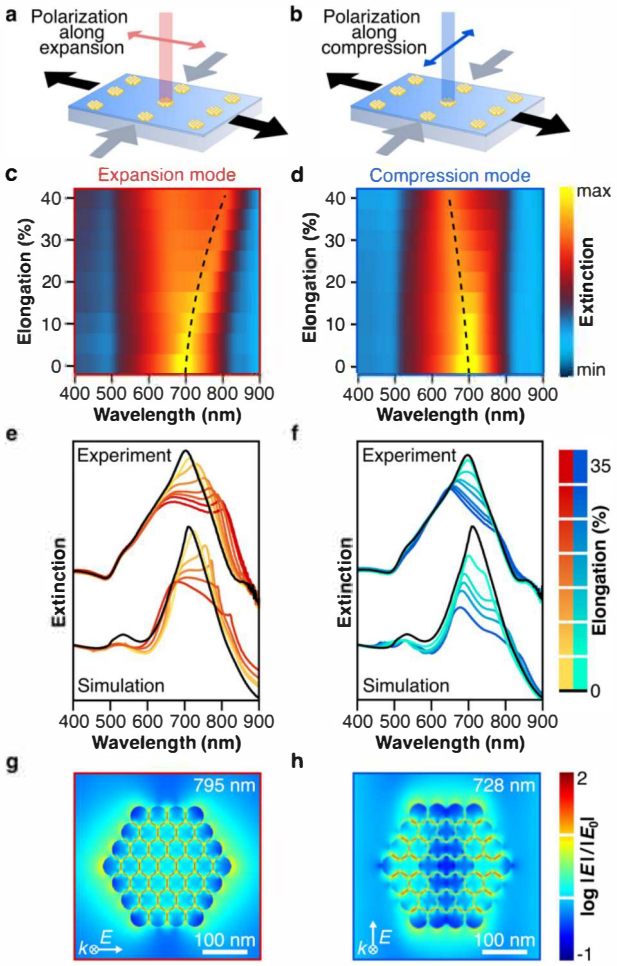

(89 × 139 mm², 300 dpi)

Figure 3. Optical changes for lattice expansion and compression during asymmetric unidirectional mechanical deformation: scheme of stretched superlattice and light polarization, along the direction of either expansion (a) or compression (b). (c,d) Experimental extinction spectra for various elongation states, according to the provided color scale. Comparison of experimental and simulated extinction spectra upon unidirectional strain and light polarized along the direction of expansion (e) and contraction (f), in stacked representation. Black curves represent the optical properties of the superlattice in pristine conditions. Electric-field enhancement maps for the expansion (g) and compression (h) modes for an array with 15% of elongation, excited at the wavelength of the resonance peaks.

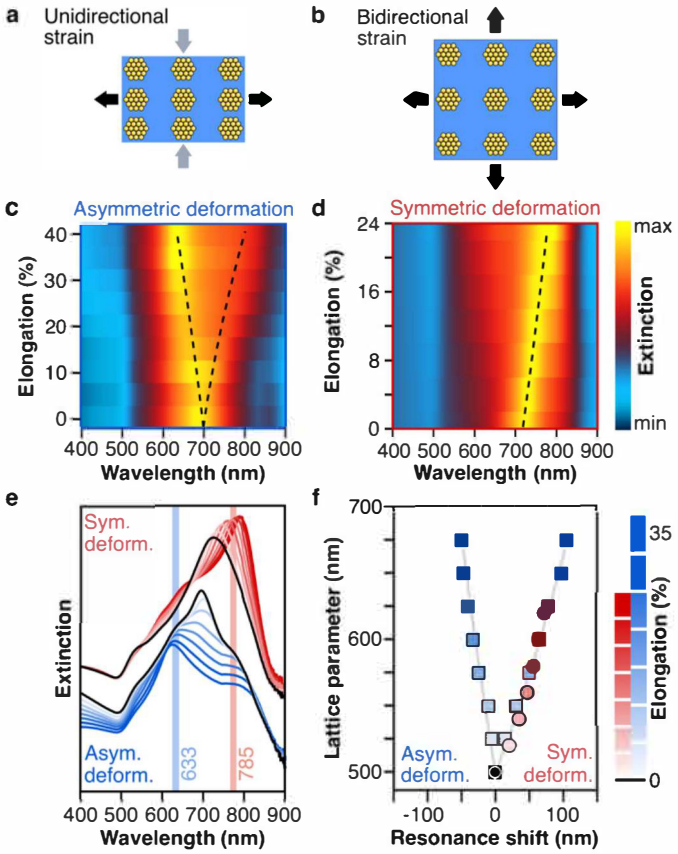

(89 × 112 mm^2, 300 dpi)

Figure 4. Optical effects of asymmetric (unidirectional) versus symmetric (bidirectional) lattice deformation: (a,b) Schematic depiction of lattice deformations. Experimental extinction maps for a 500 nm superlattice under asymmetric (c) and symmetric (d) strain. Dashed lines indicate mode shifts. (e) Corresponding experimental extinction spectra and (f) comparison of the resonance shifts under asymmetric (blue squares) and symmetric deformations (red circles).

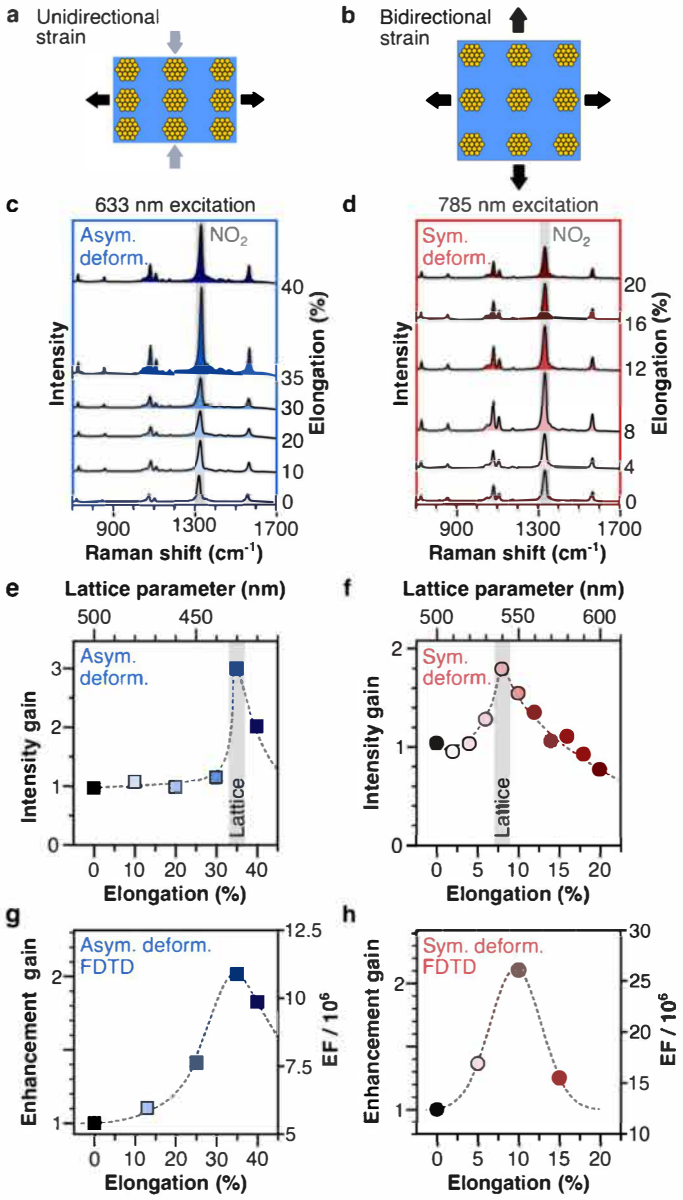

(89 × 158 mm^2, 300 dpi)

Figure 5. Mechanical tuning of SERS performance as a function of mode-matching: Schematic drawings of asymmetrically (a) or symmetrically (b) deformed superlattices. Stacked SERS spectra of an NTP-labeled superlattice under unidirectional stretching at 633 nm excitation (c), and under bidirectional stretching at 785 nm excitation (d). (e,f) Experimental SERS enhancement as a function of lattice elongation, obtained from the intensity of the NO_2 stretching vibration (gray highlighted area in c,d) and normalized to the intensity in unstretched state. Enhancement was found to peak at resonant conditions between lattice plasmons and excitation lines. Dashed lines serve as guide to the eye. Gray highlighted areas indicate a spectral matching of the lattice modes with the corresponding excitation lines (*cf.* Figure 2e). (g,h) Gain in enhancement predicted by FDTD modeling.

Table of contents entry (53 words): Changes in periodicity of superlattices of templated self-assembled plasmonic nanoparticles on flexible supports by macroscopic strain enable active mechano-optical finetuning of lattice plasmons. Both lattice expansions and contractions can adjust a single predefined lattice structure to either red-shifted or blue-shifted excitation lines, granting an additional gain in SERS performance when tuned to resonance.

M. Charconnet, C. Kuttner,* J. Plou, J. L. Garcia-Pomar, A. Mihi, L. M. Liz-Marzán,* A. Seifert*

Mechanically Tunable Lattice-Plasmon Resonances by Templated Self-Assembled Superlattices for Multi-Wavelength Surface-Enhanced Raman Spectroscopy

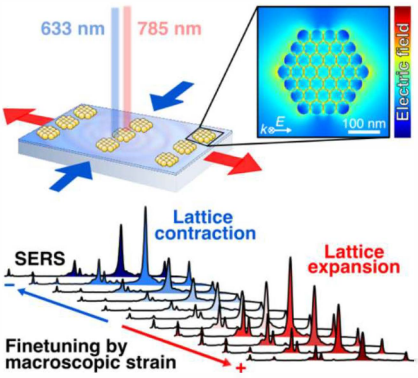

(55 × 50 mm^2, 300 dpi)

Supporting Information

Mechanically Tunable Lattice-Plasmon Resonances by Templated Self-Assembled Superlattices for Multi-Wavelength Surface-Enhanced Raman Spectroscopy

Mathias Charconnet,[#,1,2] Christian Kuttner,[#,,2] Javier Plou,[2] Juan Luis Garcia-Pomar,[3] Augustín Mihi,[4] Luis M. Liz-Marzán,[*,2,5,6,7] and Andreas Seifert[*,1,5]*

[1] CIC nanoGUNE BRTA, 20018 San Sebastián, Spain.
[2] CIC biomaGUNE, Basque Research and Technology Alliance (BRTA), 20014 Donostia-San Sebastián, Spain.
[3] INL – International Iberian Nanotechnology Laboratory, 4715-330 Braga, Portugal.
[4] Instituto de Ciencia de Materiales de Barcelona (ICMAB-CSIC), 08193 Bellaterra, Spain.
[5] IKERBASQUE, Basque Foundation for Science, 48009 Bilbao, Spain.
[6] Centro de Investigación en Red de Bioingeniería, Biomateriales y Nanomedicina (CIBER-BBN), 20014 Donostia-San Sebastián, Spain.
[7] Department of Applied Chemistry, University of the Basque Country (EHU-UPV), 20018 San Sebastián, Spain.
[#] These authors contributed equally.
[*] christian.kuttner@googlemail.com; llizmarzan@cicbiomagune.es; a.seifert@nanogune.eu.

Table of Contents:

Section S1: Materials and methods (page S2)

Section S2: Structural characterization by electron microscopy (page S5)

Section S3: Statistical analysis of gap sizes in (page S6)

Section S4: Optical characterization and numerical simulations (page S8)

Section S5: Additional SERS experiments (page S14)

SI References (page S15)

Section S1: Materials and methods

Materials. $HAuCl_4 \cdot 3\ H_2O$ (≥99.9%, trace metal basis) and 4-nitrothiophenol (96%, NTP) were purchased from Alfa Aesar. Sodium borohydride (ReagentPlus®, ≥99%, $NaBH_4$), cetyltrimethylammonium chloride (≥98%, CTAC), L-ascorbic acid (ACS reagents, ≥99%, AA), poly(ethylene glycol) methyl ether thiol average (M_n 6 kg mol^{-1}, PEG-6K), polydimethylsiloxane (Sylgard® 184, PDMS), polyethyleneimine (M_w 25 kg mol^{-1}, PEI, highly branched), and sodium hypochlorite (6 - 14% active chlorine, Emplura®, NaOCl) were purchased from Sigma-Aldrich. All solutions, except $HAuCl_4$ and CTAC, were prepared immediately before use. Purified Milli-Q water was used in all experiments (Millipore, 18.2 MΩ cm). Glassware was cleaned with *aqua regia* and rinsed extensively with Milli-Q water before use.

Nanoparticle synthesis and functionalization. Nanospheres were synthesized by seeded growth as reported recently.[S1] First, small seeds of 2 nm were prepared by adding $HAuCl_4$ (50 µL, 0.05 M) to a CTAC solution (5 mL, 100 mM). Subsequently, $NaBH_4$ (200 µL, 0.02 M, *i.e.*, 7.5 mg in 10 mL) was added under vigorous stirring. After 3 min, the mixture was diluted 10 times by a CTAC solution (100 mM). Then, the small seeds were overgrown to 10 nm nanospheres: For this purpose, the small seeds (900 µL) were added to a mixture of AA (40 µL, 0.1 M) and CTAC (10 mL, 25 mM). Next, $HAuCl_4$ (50 µL, 0.05 M) was added under vigorous stirring. The 10 nm seeds showed an LSPR at 520 nm. The dispersion was left undisturbed for at least 1 h. Afterward, the nanospheres were centrifuged (19,300 rcf, 12 cm rotor) and washed at least 3 times with CTAC solution (25 mM). Afterward, the 10 nm sized nanospheres were overgrown to larger nanospheres: First, the nanospheres (125 µL) were added to a solution AA (40 µL, 0.1 M) and CTAC (10 mL, 25 mM). Subsequently, $HAuCl_4$ (50 µL, 0.05 M) was added. The resulting nanoparticles had rough edges, which were removed by oxidative etching. For this, a diluted solution of sodium hypochlorite (10 µL, 1 to 1.5% of available chlorine) and 10 min later $HAuCl_4$ (5 µL, 0.05 M) was added under continued stirring. After 30 min, the final nanospheres were centrifugated (3100 rcf, 12 cm rotor, 15 min) and redispersed in CTAC solution (500 µM). The final NPs were concentrated to *ca.* 5 mM Au^0 in a solution of CTAC (500 µM). Functionalization was done by addition of PEG (1 mg mL^{-1}) and stirring overnight at room temperature (RT). Excess unbound PEG was removed by repeated centrifugation (3100 rcf, 12 cm rotor, 15 min) and redispersion of the sedimented NPs in CTAC (500 µM).

Preparation of PDMS target substrates: PDMS was prepared by casting of a cross-linker/prepolymer mixture (1:15, 25 g) in a levelled polystyrene dish (10 cm diameter) and degassing in vacuum. The PDMS mixture was cross-linked in two steps: 24 h at RT and then 5 h at 80 °C. The cured PDMS was cut into 1 × 4.5 cm^2 strips and incubated in a fresh PEI solution (10 mg mL^{-1}), to promote the adhesion between nanoparticles and PDMS substrate.[S2] After 3 h, the strips were removed, washed with water, dried under a N_2 stream, and directly used as target substrates.

Preparation of PDMS template: Soft PDMS templates were fabricated by pouring a cross-linker/prepolymer mixture (1:10) onto patterned silicon masters or their negative replicas with

OrmoStamp® (Microresist Technology).[S3,S4] The arrangement of the holes in the template is rotated by about 45° with respect to the template's edges. The mixtures were degassed for 2 h to increase the percolation of the polymer inside the nanostructures and then cured (45 min, 100 °C).

Templated self-assembly of superlattices. Superlattices were prepared as reported recently.[S5] A 2 µL droplet of nanoparticle dispersion (30 mM Au^0 calculated from the extinction at 400 nm, 66% EtOH, 200 µM CTAC) is cast on a PDMS target substrate. After 40 s of waiting time, a nanostructured PDMS stamp was added on top of the droplet. This template featured a square lattice of holes of 270 nm with a spacing of 500 nm.[S6] After 2 h and complete evaporation of the liquid, the PDMS template was carefully lifted off the flexible PDMS substrate. The resulting dried and nanostructured film consists of a nanoparticle superlattice representing the inverse structure of the template. Due to the orientation of the hole structure in the template, the templated samples had to be stretched diagonally (with respect to the printed area) to deform the square lattice along its principal axes.

Fabrication of disorganized sample (as reference). To fabricate disorganized samples of disordered Au nanoparticles, Au^0 dispersion (100 µL, 4 mM, 40 nm sized PEG-coated nanospheres) was drop-cast on a PDMS target substrate and allowed to dry (3 h, RT).

UV/vis/NIR spectroscopy. Extinction spectra of colloidal dispersions were recorded with an Agilent 8453 UV/vis spectrophotometer, using polystyrene cuvettes. Extinction spectra of dry samples were collected using a Carry 5000 UV-vis spectrometer (Agilent). Samples were mounted on custom-made stretching devices and measured under normal incidence. The measurements were performed in such a way that the same surface area was probed during strain experiments.

Electron microscopy. Scanning electron microscopy was performed using an environmental SEM (FEI Quanta 250). To investigate the structural changes induced upon strain *in-situ*, the sample was clamped in a custom-made stretching device (approx. 8×4×1 cm^3) and fixed on a motorized stage inside the vacuum chamber. To increase/decrease the strain, vacuum was interrupted, and strain was changed manually with a micrometer screw ratchet, while positioning of the sample remained unchanged. Extra precaution was necessary to image the flexible superlattices because of an accumulation of charges at the surface even at low voltages. Already, at 20 kV (15,000× magnification), deformations of the superlattice structure were visible owing to charging (Figure S3). For that reason, overview images were recorded at an acceleration voltage of 10 kV with an integration time of 1 µs per line at a magnification of 16,000×. Detail images, resolving the NPs within the clusters, were taken at 20 kV with an integration time of 10 µs per line at a magnification of 30,000×.

SERS. For SERS experiments, the samples were incubated in an aqueous solution of NTP (1 µM, 2 h), prepared freshly from a stock solution in EtOH (10 mM). After incubation, the samples were thoroughly rinsed with water to remove the excess NTP molecules that did not bind to the AuNPs and dried with N_2 flow. Spectra with 633 nm excitation were obtained using a Renishaw

inVia reflex equipped with a stigmatic single-pass spectrometer, a Peltier-cooled CCD detector (1024 × 512 px^2), a 1800 grooves mm^{-1} grating, a HeNe laser as excitation line (633 nm, 0.55 mW), and a 50× lens (LWD, NA 0.5) yielding a spot size of around 20×20 µm^2 (approx. 40×40 illuminated substructures). Spectra with 785 nm excitation (Ondax SureLock mini-benchtop stabilized laser, 10 mW) were obtained using a custom-made Raman system with a lens (10 mm focal length, NA 0.38) and spot size of ca. 150×150 µm^2 (approx. 300×300 illuminated substructures). Due to the finite size of the illuminated sample area, it can be expected that a minimum number of substructures must be excited (e.g., 30×30 subunits[S7]) to fully exploit the potential of lattice plasmon coupling through periodic superstructuring. For both excitation wavelengths, the spot size was chosen to achieve such a minimum number and similar spot measurements were performed to provide quantitative data for the change in SERS performance during stretching experiments and at defined elongation states. To obtain statistically relevant data, data for extended sample areas of 200 × 200 µm^2 were collected by surface mapping. During stretching experiments, the focus was readjusted after each elongation step. The focus plane was defined as the *z*-height yielding maximum signal intensity.

Electromagnetic simulations. Numerical calculations were performed using Lumerical FDTD Solutions (version 2020a R7). Clusters of NPs with a diameter of 40 nm were modeled with interparticle distances of 1 nm, using a non-uniform mesh. Each particle was enclosed in a shell of 0.5 nm thickness with a refractive index of 1.46 to emulate PEG. The PDMS substrate was modeled as a smooth surface with a refractive index of 1.4. For gold, tabulated data by Johnson and Christy was used.[S8] For the calculation of extinction cross sections, a polarized planewave source was injected at normal incidence in a range of 400 to 900 nm. Two orientations of the cluster (0° and 90° rotation) have been considered and averaged. The enhancement factor (EF) of SERS was defined as the product of the enhancements of the field intensity $|E|^2/E_0|^2$ at the incident wavelength of excitation and at the corresponding Stokes-shifted frequency of the vibrational mode of interest (Equation 3).[S9,S10] The electric-field enhancements have been calculated from the surface integral of the intensity enhancement on the surface of the NPs and normalized by the total number of particles per µm^2. The surface-averaged electric field $\langle|E|^2/|E_0|^2\rangle$ was defined as

$$\left\langle \frac{|E|^2}{|E_0|^2} \right\rangle = \frac{\iint \frac{|E|^2}{|E_0|^2} \mathrm{d}S}{\iint \mathrm{d}S} \tag{S1}$$

Since the experimental light source is a partially depolarized beam, an average of different polarizations and their respective cluster rotations was considered in this case. For the isolated cluster a total-field scattered-field (TFSF) source with the same intensity by unit area was used for the periodic system to calculate the absorption cross section.

Section S2: Structural characterization by electron microscopy

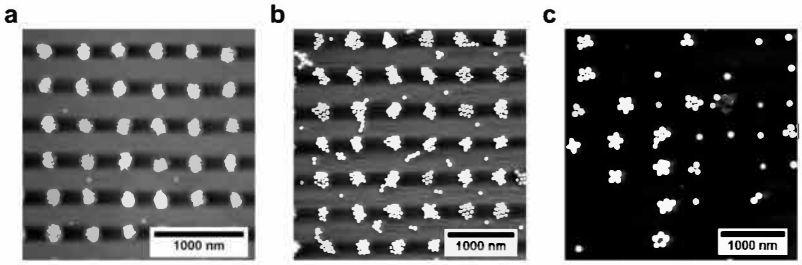

Figure S1. Examples of e-SEM images of superlattices with nanospheres of (a) 40 nm, (b) 65 nm, and (c) 105 nm in diameter. Best transfer was achieved for smallest particles.

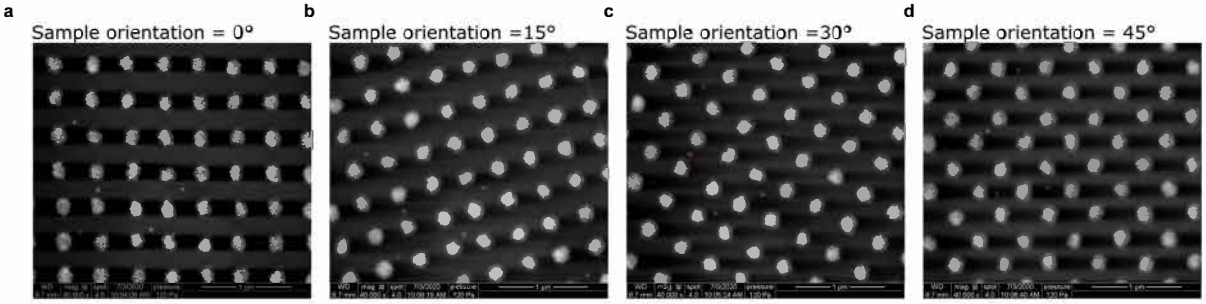

Figure S2. Examples of e-SEM images of a superlattice with period of 500 nm for different sample orientations. The effect of surface charging can be observed as dark shadows along the scanning direction. By changing the sample orientation, it can be clearly shown that these are merely imaging artifacts that do not indicate changes in the structures or the sample surface.

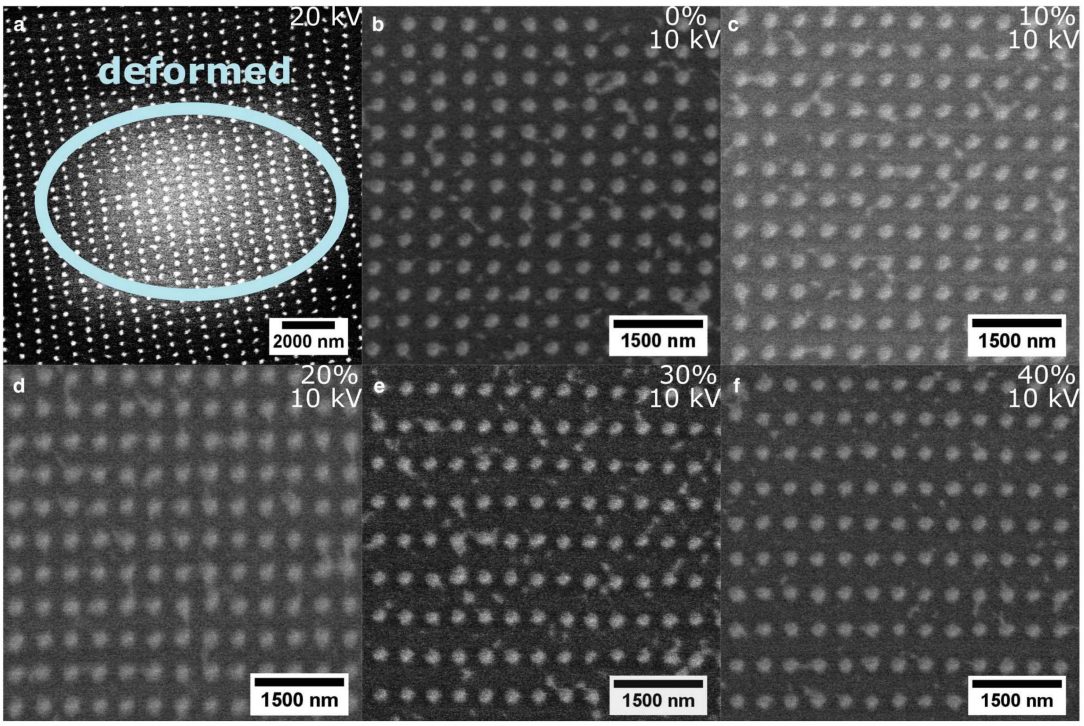

Figure S3. Examples of e-SEM images of a 500 nm superlattice under unidirectional stretching. (a) The overview image at 20 kV shows a deformation of the sample surface, indicated in blue, owing to charging effects. (b-f) Detail images taken at 10 kV allow for quantification of the period of the superlattice at different elongation states.

Section S3: Statistical analysis of gap sizes in clusters

In this section, $\langle x \rangle$ refers to the *mean* of the values x, Δx denotes the *standard deviation* of their Gaussian distribution, and $\Delta\langle x \rangle$ represents the *standard error*, *i.e.*, the error of the mean $\langle x \rangle$.

Measurement of particle size: The diameters of the individual NPs were measured using TEM images taken in different regions of the TEM grid (Figure S4a). The resolution of TEM allows a quantification of the average diameter with sub-nm precision (Figure S4b).

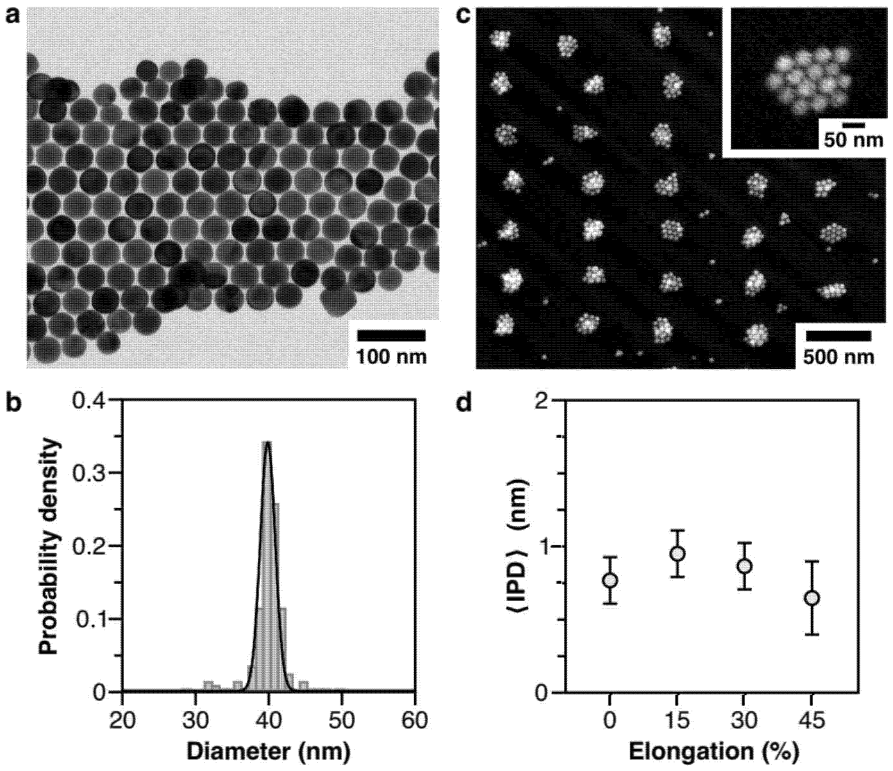

Figure S4. (a) TEM images of nanospheres used for the fabrication of superlattices and the corresponding (b) size distribution (189 particles with a diameter of $\langle D \rangle \pm \Delta D = 39.7 \pm 2.4$ nm and $\Delta\langle D \rangle = 0.18$ nm); (c) typical e-SEM image of a superlattice under 30% unidirectional stretching, showing no indication of cluster fragmentation or breakup; (d) mean interparticle distances evaluated by image analysis and corresponding uncertainties, versus substrate elongation (Table S1).

Table S1. Overview of the parameters obtained from particle distance measurements of M lines.

Elongation (%)	Lines M	⟨IPD⟩ (nm)	Δ⟨IPD⟩ (nm)
0	117	0.76	0.16
15	148	0.94	0.16
30	131	0.86	0.16
45	53	0.65	0.25

Measurement of interparticle distance values: The interparticle distance (IPD) was evaluated from e-SEM images. A direct measurement of the gaps is highly challenging owing to the resolution limit of the environmental SEM and the sample's susceptibility to accumulate

charges. For this reason, we evaluated the gap sizes indirectly by measuring linear oligomers within clusters, *i.e.*, lines/chains of particles. By preferentially measuring the length of particle lines oriented along the direction of stretching, we studied the impact of substrate deformation (by unidirectional stretching) on the average interparticle distances within clusters (*e.g.*, sample at 30% elongation, Figure S4c). Each line corresponds to a separate determination of the gap size IPD with its respective uncertainty. The description implies equal distributed gap sizes within each measured line as calculated by

$$\mathrm{IPD} = (k-1)^{-1}\left(L - \sum_{\mathrm{j}=1}^{k} D_{\mathrm{j}}\right) \approx (k-1)^{-1}(L - k\langle D\rangle), \tag{S2}$$

where L is the total measured length of the respective line, composed of k particles of diameters D_{j}. The gap sizes per line are determined by the sum over all gaps per line, this is the difference of each line length L and the presumed length contribution by k particles $\Sigma D_{\mathrm{j}} \approx k\,\langle D\rangle$, divided by the number of gaps $k-1$. Averaging the gap sizes of all lines with the same number of particles, consisting of $(k-1)$ m_{k} gaps, yields

$$\langle \mathrm{IPD_k}\rangle = \left((k-1)m_{\mathrm{k}}\right)^{-1} \sum_{\mathrm{j}=1}^{m_{\mathrm{k}}} \left(L_{\mathrm{kj}} - k\langle D\rangle\right), \tag{S3}$$

with L_{kj} being the length of the m_{k} individual chains with k particles. The uncertainty of $\langle \mathrm{IPD_k}\rangle$ from Equation S3 can be calculated by error propagation as

$$\Delta\langle \mathrm{IPD_k}\rangle = \left((k-1)m_{\mathrm{k}}\right)^{-1} \sqrt{m_{\mathrm{k}}(\Delta L)^2 + k m_{\mathrm{k}}(\Delta D)^2}. \tag{S4}$$

Equation S4 considers $\langle D\rangle$ as a statistical quantity with the variation $\Delta\langle D\rangle = \frac{\Delta D}{\sqrt{k}}$ and that the error of chain length determination ΔL is the same for all chains. ΔL is mostly driven by the resolution of e-SEM, and we assume a realistic value of ΔL = 1 nm for all lines. The uncertainty of the particle size derived from TEM imaging was determined to ΔD = 2.4 nm (*cf.* Figure S2b). The ratio between the term corresponding to D and the one corresponding to L under the square root in Equation S4 ranges from 17 to 35 for chain lengths between 3 and 6 particles, as in the present case. The contribution of the length error can thus be neglected, resulting in

$$\Delta\langle \mathrm{IPD_k}\rangle = (k-1)^{-1} \sqrt{\frac{k}{m_{\mathrm{k}}}}\,\Delta D \tag{S5}$$

Equation 3 leads to the averaged interparticle distance over all gaps and all chains

$$\langle \mathrm{IPD}\rangle = N_{\mathrm{g}}^{-1} \sum_{\mathrm{k}} (k-1) m_{\mathrm{k}} \langle \mathrm{IPD_k}\rangle, \tag{S6}$$

thereby taking into account the total number of gaps $N_{\mathrm{g}} = \sum_{\mathrm{k}} (k-1)\, m_{\mathrm{k}}$. Error propagation delivers the final uncertainty of the averaged gaps from the complete sample.

$$\Delta\langle \mathrm{IPD}\rangle = N_{\mathrm{g}}^{-1} \sqrt{\sum_{\mathrm{k}} \left((k-1)m_{\mathrm{k}}\right)^2 \Delta\langle \mathrm{IPD_k}\rangle^2} \tag{S7}$$

Inserting Equation S5 into S7 yields the uncertainty of the total averaged interparticle distance $\langle \mathrm{IPD}\rangle$ just by the error ΔD of the particle size and represents a weighted standard error of ΔD,

$$\Delta\langle \mathrm{IPD}\rangle = N_{\mathrm{g}}^{-1} \Delta D \sqrt{\sum_{\mathrm{k}} k m_{\mathrm{k}}}, \tag{S8}$$

where the summation again is over all chain lengths (number of particles k). The obtained results are summarized in Table S1 and plotted in Figure S4d.

Section S4: Optical properties and numerical simulations

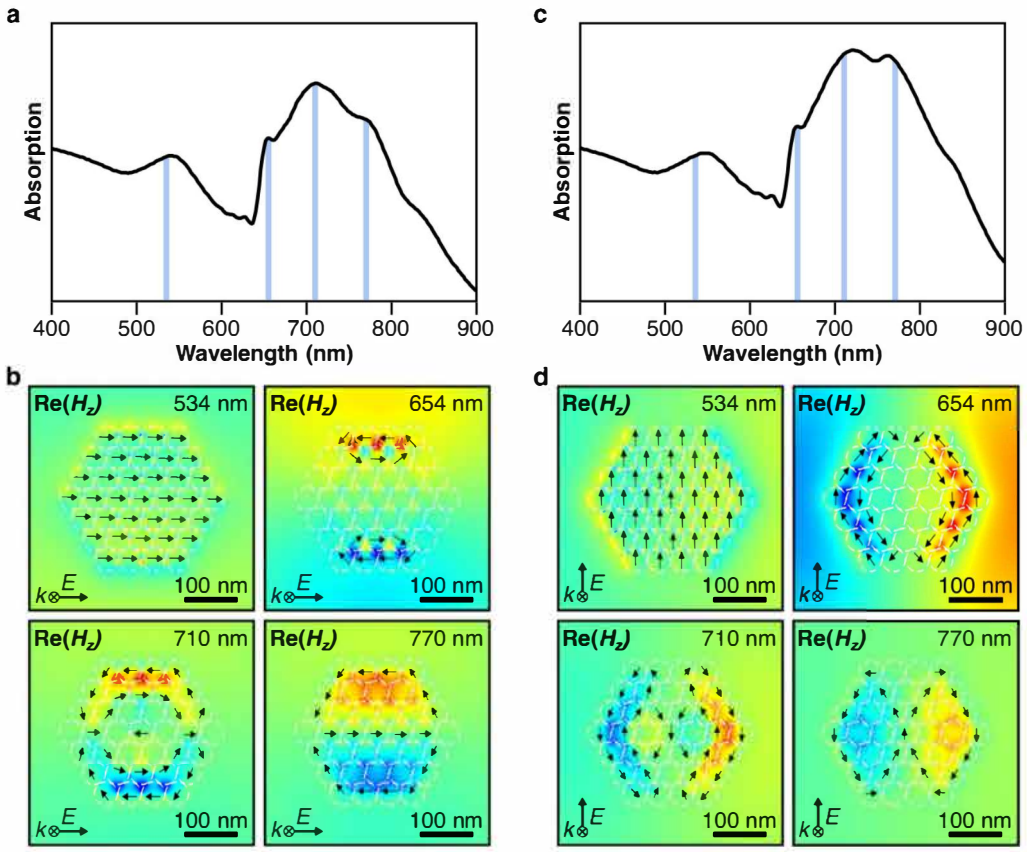

Figure S5. Electromagnetic simulations of an isolated cluster for polarization along (a,b) *x* and (c,d) *y* direction: (a,c) absorption cross sections and (b,d) snapshots of different resonance modes illustrated by the real part of the vertical magnetic field H_z. The black arrows indicate the direction of the electric current. The plasmonic responses of the primary resonances between 654 and 770 nm are considerably more intense than the secondary resonances at 534 nm. Due to the lack of plasmonic interaction between the NPs, lattice tuning to an excitation in the green (532 nm) is not meaningful for this substructure design and SERS efficiency would be limited.

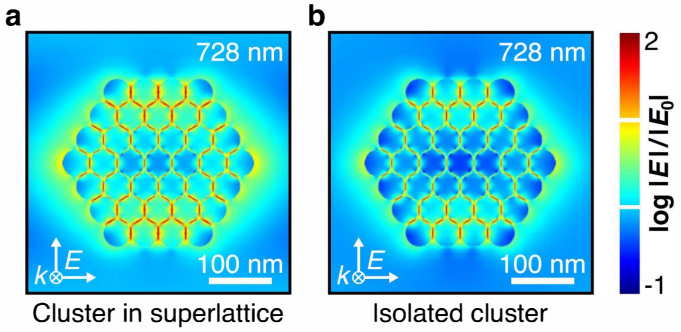

Figure S6. Comparison of the near-field enhancement of a cluster in a periodic arrangement (left) with a lattice parameter of 500 nm compared to an isolated cluster (right); excited at 728 nm using a light source with an intensity normalized by area. In periodic arrangement the field enhancement within the gaps is much more pronounced (red areas).

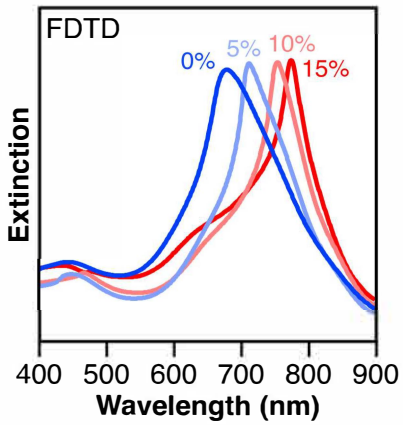

Figure S7. Simulated extinction spectra of a superlattice with an initial periodicity of 500 nm, which is deformed bidirectionally by 5%, 10% and 15% giving lattice parameters of 525 nm, 550 nm, and 600 nm, respectively.

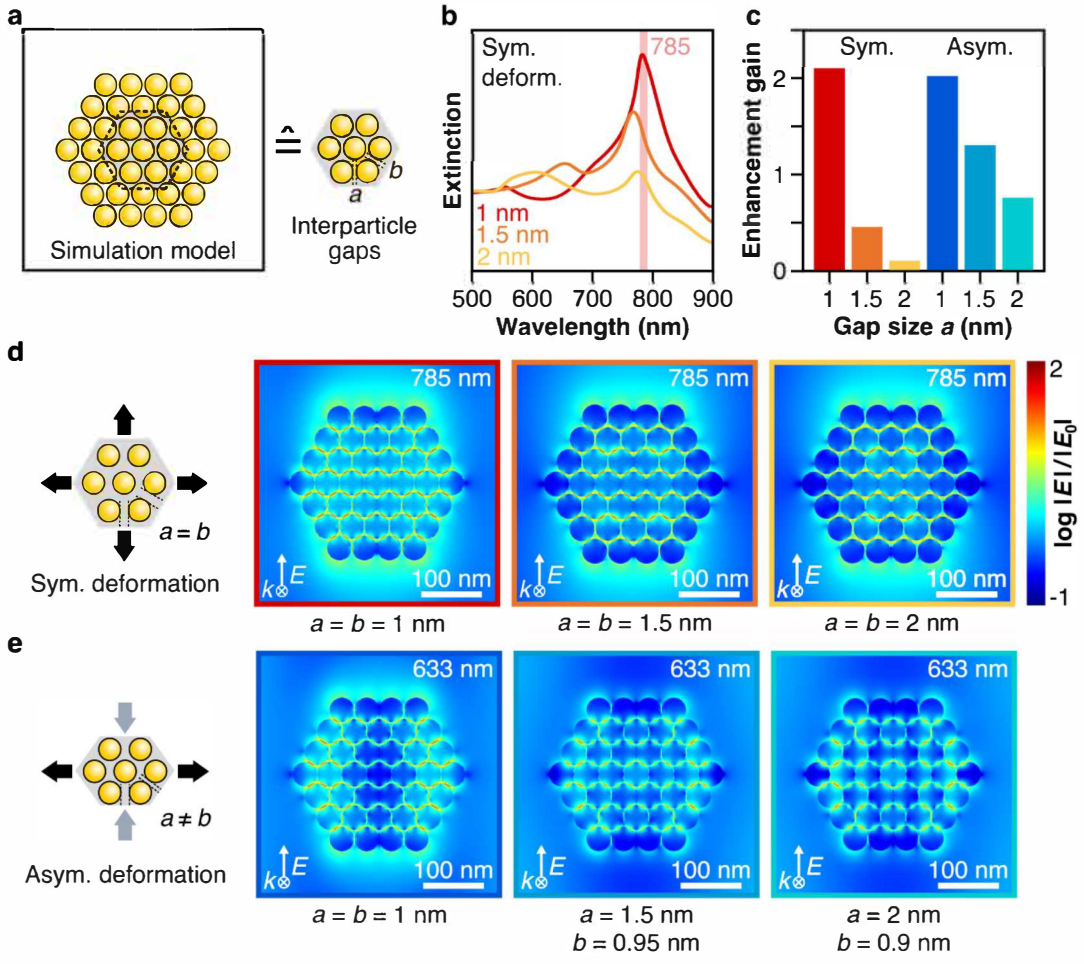

Figure S8. Impact of substructure spacings on the lattice plasmon and near-field enhancement: (a) Schematic model of a cluster (with gap sizes *a* and *b*) in periodic boundaries with periods tuned for maximum enhancement (550 nm for sym.; 675 and 412.5 nm for asym.); (c) change in extinction for a symmetric increase of gap size; (c) reduction in near-field enhancement gain by symmetric or asymmetric deformations of gap size. Electric-field enhancement maps for (d) sym. deformations excited at 785 nm and (e) asym. deformations excited at 633 nm.

Hypothetical deformation of the substructure

Relationship of gap sizes a and b for a hypothetical asymmetric deformation of the substructure: In the initial state without deformation, three adjacent particles form an equilateral triangle, with an edge length given by two particle radii (r_{NP} = 20 nm) and the respective interparticle gap *a* or *b*. Thus, the length of the base edge *E* is a function of *a*. The triangle's height *H* on this base side is $3^{0.5}/2 \cdot E$. The length of the compressed edges *C* is given by

$$C = (0.5 \cdot E) / \cos(\alpha) \quad \text{with} \quad \alpha = \tan^{-1}((H - \Delta H)/(0.5 \cdot E)) \tag{S9}$$

Consequently, the gap sizes *b* along the compressed edges equal $C - 2\, r_{NP}$. Due to transverse contraction, *H*, *C*, and *b* will be compressed upon a stretching of *E* by increasing *a*. Assuming a Poisson's ratio of 0.5 ($\Delta H = -0.5 \cdot \Delta E$), the values listed in Table S2 are obtained.

Table S2. Ratio of gap sizes during a hypothetical asymmetric deformation of the substructure.

a (nm)	*b* (nm)	*E* (nm)	*H* - Δ*H* (nm)	*C* (nm)
1	1	41	35.5	41
1.5	0.95	41.5	35.3	40.95
2	0.9	42	35.1	40.9

Already small changes in interparticle distances within clusters result in significant changes of the optical properties (Fig. S8b). The primary lattice plasmon shifts slightly and, more importantly, its intensity drops by a factor of 2. The latter indicates that already a gap increase of 0.5 nm would significantly weaken the plasmonic interactions. Figure S8c compares the enhancement gains in the near-field upon varying the gap sizes. Just as with the optical data, significant changes in the field distribution can be seen. When the distances are increased to 1.5 and 2 nm, the overall field strength is weakened, and the distribution of hotspots is less widespread. This confirms that even small gap changes critically affect plasmonic coupling and thus reduce SERS activity. Since our experiments did not show these detrimental effects, even after several stretching cycles, we can safely assume that the gaps within the clusters are robust.

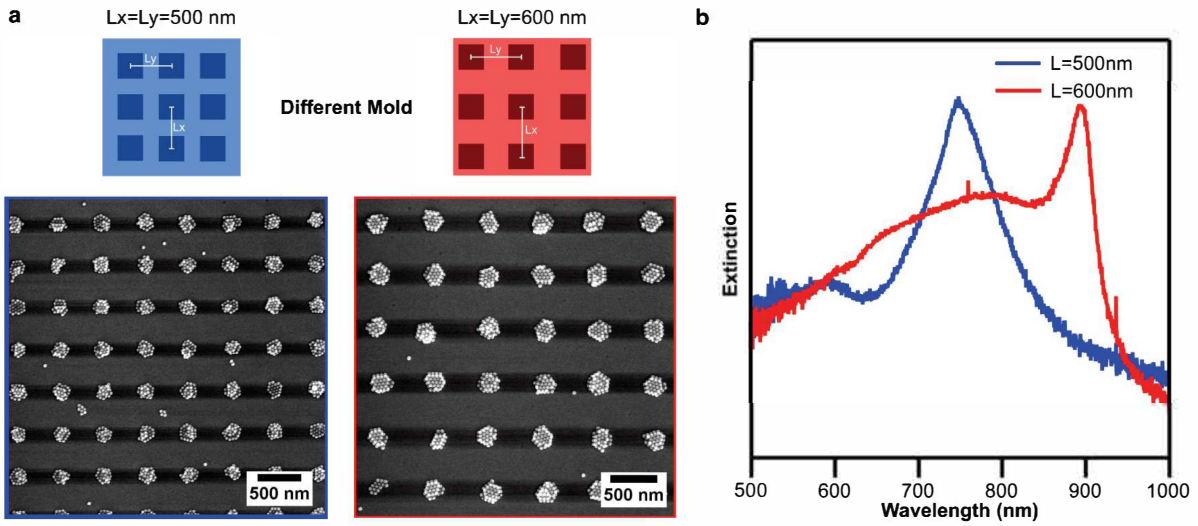

Figure S9. Optical properties of reference superlattices with 500 and 600 nm periods prepared on rigid substrates (glass) using different molds: (a) e-SEM images and (b) extinction spectra.

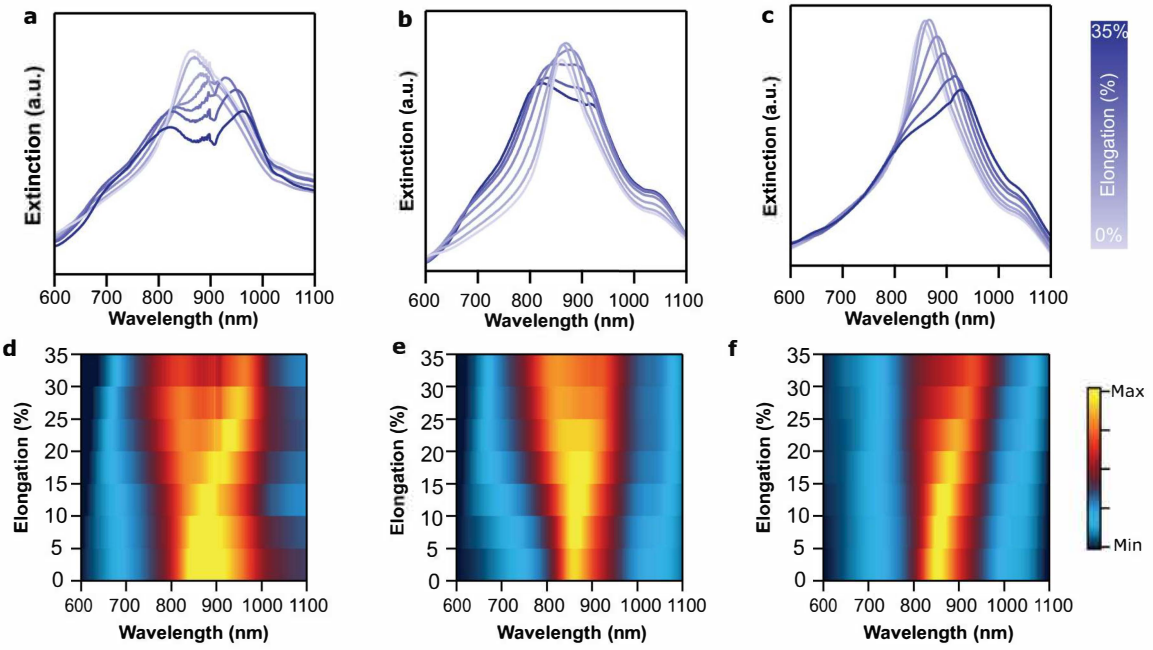

Figure S10. Extinction spectra of a superlattice with a period of 600 nm at different elongation states using (a) unpolarized light (this is without using a linear polarizer), (b) light polarized along the contraction axis (c) along the elongation axis. Corresponding extinction maps for (d) unpolarized light, (e) light polarized along the contraction axis, (f) light polarized along the elongation axis.

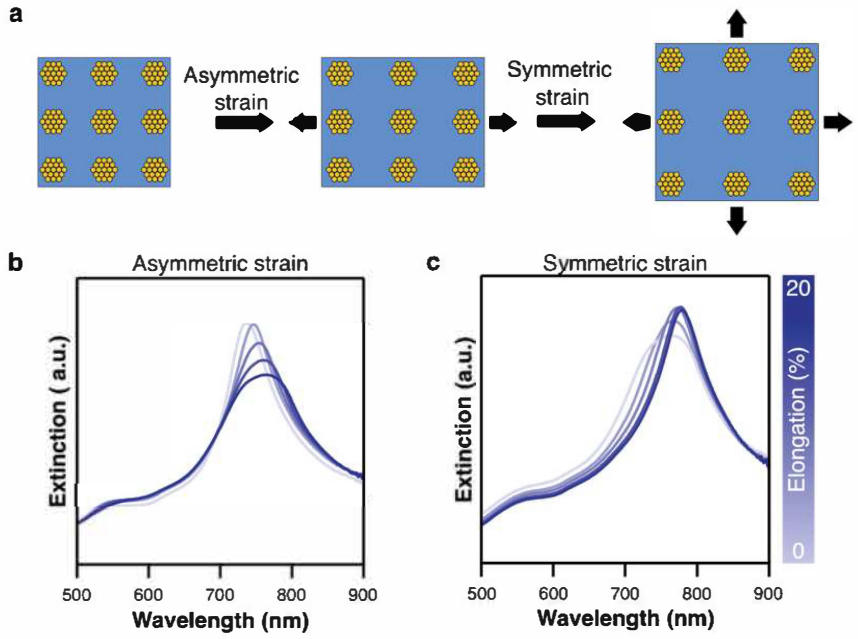

Figure S11. (a) Two-step stretching process: First, the sample is stretched (in *x*-direction) to a rectangular lattice, without contraction in *y*-direction, by using a 2D stretching device. Then, the sample is stretched in *y*-direction to form a square lattice. Extinction spectra of a 500 nm superlattice (b) stretched to a rectangular lattice without contraction and (c) stretched from a rectangular lattice to a square lattice.

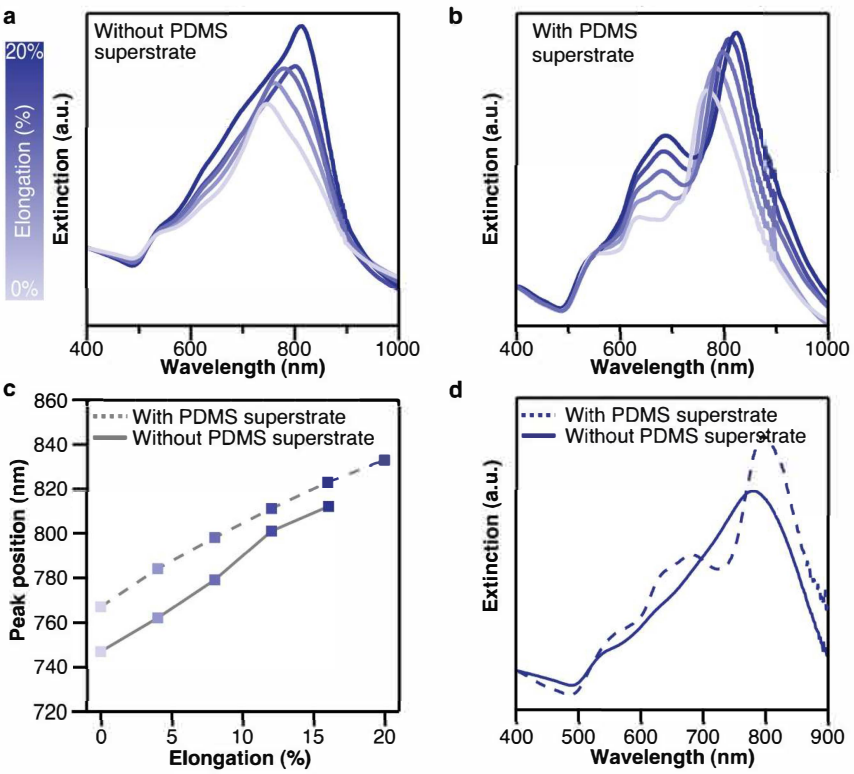

Figure S12. Extinction properties of superlattice with a period of 500 nm (a) with and (b) without an additional layer of PDMS (as superstrate) cast on top of the sample to provide a homogenous refractive index environment. (c) Evolution of the lattice plasmon peaks under stretching with and without the PDMS superstrate. (d) Comparison of extinction spectra between a sample with and without PDMS superstrate at 8% elongation. The secondary peak at around 650 nm could be attributed to plasmonic contributions of higher order.

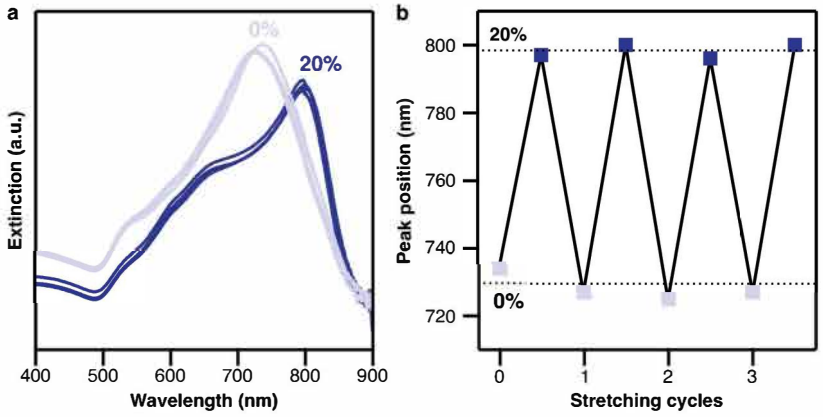

Figure S13. Repeatability test: (a) Extinction spectra of a 500 nm period superlattice after various stretching cycles. (b) Evolution of the lattice plasmon peak position for successive switching between 0% and 20% elongation states.

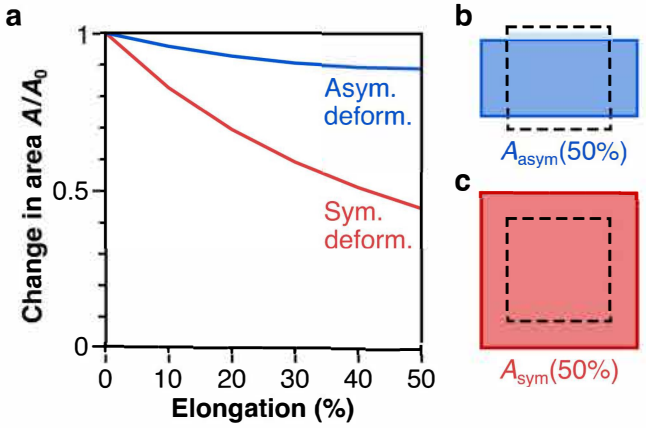

Figure S14. (a) Change in surface area upon asymmetric (blue) and symmetric stretching (red) of a material with a Poisson's ratio of 0.5, estimated by Equation S10 and S11, respectively; (b,c) illustration of the effect of elongation on a schematic substrate surface with an exemplary elongation of 50% (colored area) versus 0% (black dashed line).

The change of surface area A at elongation $\Delta L/L$ in reference to the area in unstretched state A_0 can be geometrically estimated (*cf.* Figure S14). In the case of asymmetric deformation (A_{asym}/A_0), this is for uniaxial strain, Poisson's ratio ν needs to be considered:

$$A_{asym}(\Delta L/L) / A_0 = (1 + \Delta L/L)\cdot(1 - \nu\cdot\Delta L/L) \quad \text{(S10)}$$

In case of a symmetrical deformation (A_{sym}/A_0) it is assumed that the substrate deforms equally both vertically and horizontally.

$$A_{sym}(\Delta L/L) / A_0 = (1 + \Delta L/L)^2 \quad \text{(S11)}$$

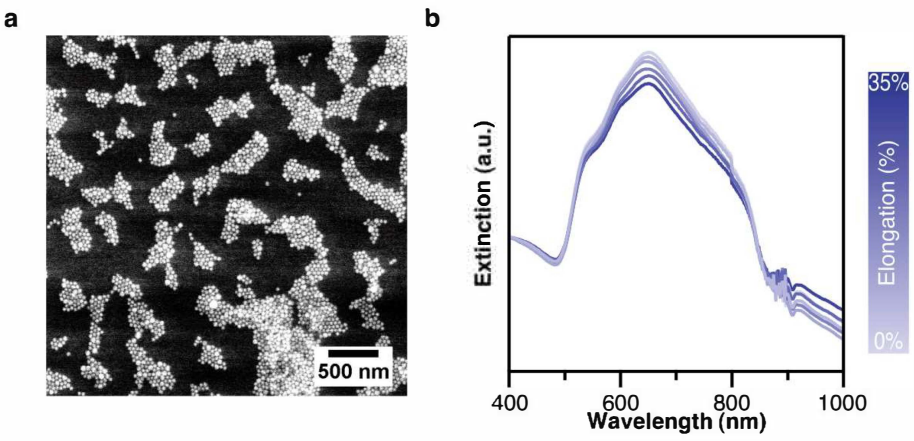

Figure S15. Reference sample of disorganized NPs: (a) e-SEM image and (b) optical properties for different elongation states. The extinction spectra remain almost unaffected by the stretching, which indicates the absence of any lattice effect, as expected.

Section S5: Additional SERS experiments

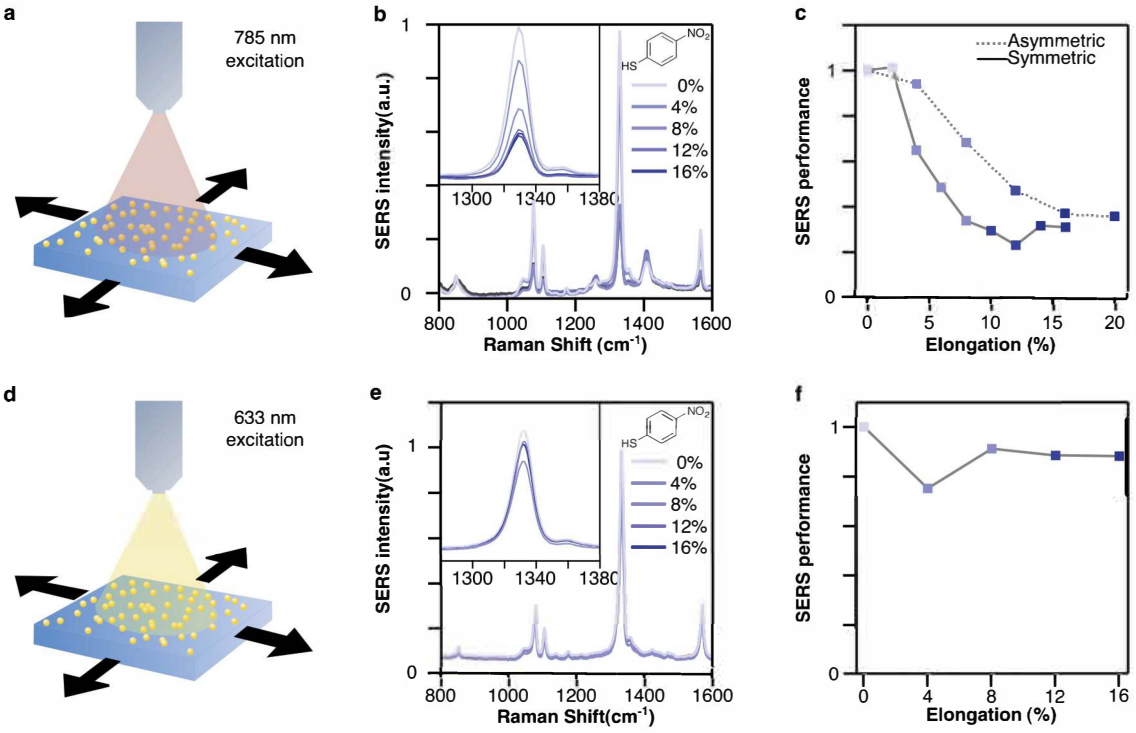

Figure S16. SERS signal of the sample of disorganized NPs at 633 and 785 nm excitation: (a) Schematic of the disorganized sample symmetrically stretched under 785 nm excitation; (b) SERS spectra and (c) signal intensity at 1330 cm^{-1} corresponding to the NO_2 signal of NTP at different elongation states under 785 nm excitation. (d) Schematic of the disorganized sample symmetrically stretched under 633 nm excitation; (e) SERS spectra and (f) signal intensity at 1330 cm^{-1} corresponding to the NO_2 signal of NTP at different elongation states under 633 nm excitation.

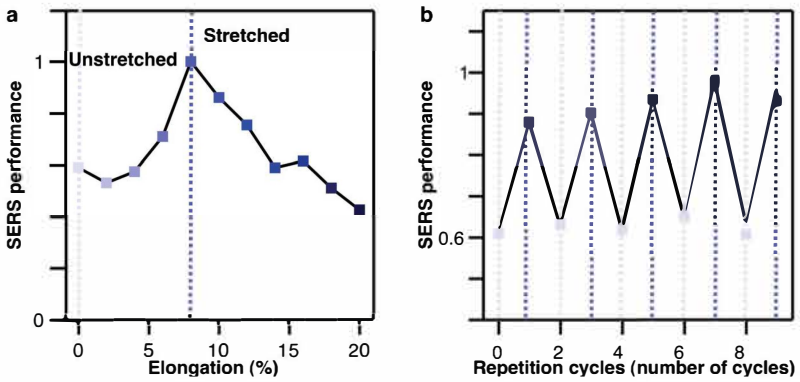

Figure S17. SERS intensity at 1330 cm^{-1} of NTP on a superlattice with a period of 500 nm: (a) for bidirectional stretching and (b) alternating between 0% and 8% stretching.

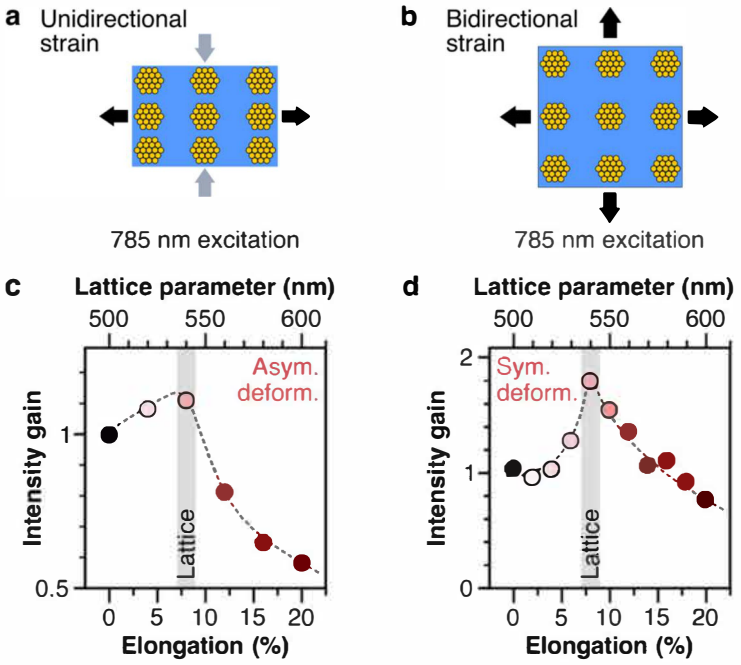

Figure S18. Comparison of the SERS performance for excitation of the expansion mode at 785 nm, for a superlattice with a period of 500 nm, deformed by asymmetric unidirectional (a,c) and symmetric bidirectional strain (b,d). SERS Intensity refers to the NO_2 signal of NTP at 1330 cm^{-1}. The gain in SERS performance upon resonant matching of the lattice plasmon with the excitation wavelength is more pronounced for symmetric deformations (by using bidirectional strain; see Fig. 5d for details).

SI References

[S1] C. Hanske, G. González-Rubio, C. Hamon, P. Formentín, E. Modin, A. Chuvilin, A. Guerrero-Martínez, L. F. Marsal, L. M. Liz-Marzán, *J. Phys. Chem. C* **2017**, *121*, 10899.

[S2] A. M. Steiner, M. Mayer, M. Seuss, S. Nikolov, K. D. Harris, A. Alexeev, C. Kuttner, T. A. F. König, A. Fery, *ACS Nano* **2017**, *11*, 8871.

[S3] Y. Xia, J. A. Rogers, K. E. Paul, G. M. Whitesides, *Chem. Rev*. **1999**, *99*, 1823.

[S4] D. Qin, Y. Xia, G. M. Whitesides, *Nat. Protoc.* **2010**, *5*, 491.

[S5] C. Hanske, E. H. Hill, D. Vila-Liarte, G. González-Rubio, C. Matricardi, A. Mihi, L. M. Liz-Marzán, *ACS Appl. Mater. Interfaces* **2019**, *11*, 11763.

[S6] S. Ni, J. Leemann, H. Wolf, L. Isa, *Faraday Discuss.* **2015**, *181*, 225.

[S7] D. Wang, M. R. Bourgeois, J. Guan, A. K. Fumani, G. C. Schatz, T. W. Odom, *ACS Photonics* **2020**, *7*, 630.

[S8] P. B. Johnson, R. W. Christy, *Phys. Rev. B* **1972**, *6*, 4370.

[S9] J. C. Fraire, L. A. Pérez, E. A. Coronado, J. Phys. Chem. C **2013**, *117*, 23090.

[S10] K. M. Kosuda, J. M. Bingham, K. L. Wustholz, R. P. Van Duyne, R. J. Groarke, *Nanostructures and Surface-Enhanced Raman Spectroscopy,* Vol. 1–5, Elsevier Ltd., **2019**.